TIME-DEPENDENT WATER VAPOR DESORPTION ISOTHERM MODEL OF HARDENED CEMENT PASTE

Jiří Rymeš[a,1], Ippei Maruyama[a, b, *], Abudushalamu Aili[a]

[a] Graduate School of Environmental Studies, Nagoya University, Nagoya, Japan

[b] Graduate School of Engineering, The University of Tokyo, Tokyo, Japan

[1] current affiliation: Researcher, Červenka Consulting s.r.o., Prague, Czech Republic

[*] corresponding author:

Jiří Rymeš: rymes@nagoya-u.jp

Ippei Maruyama: i.maruyama@nagoya-u.jp

Abudushalamu Aili: aili.abudushalamu@d.mbox.nagoya-u.ac.jp

ABSTRACT

This study aims to enhance moisture transport modeling by elucidating the so-called anomalous water diffusion in cementitious materials. Water desorption isotherms are measured from samples at various drying stages using techniques with different durations to quantify the impact of the drying duration on the water sorption ability. A single water sorption isotherm does not solely give a relationship between the water content and relative humidity but also represents the state of microstructure. The continuous evolution of a desorption isotherm due to drying-induced microstructural rearrangement is demonstrated. For numerical modeling, the microstructural alteration can be explicitly considered through a dynamic desorption isotherm

model, which governs the local thermodynamic equilibrium at the capillary meniscus. This approach is implemented into a multiphase transport code, whose ability to predict drying is validated using literature data. Finally, the effect of prolonged drying on the colloidal nature of the calcium-silicate-hydrate gel is discussed.

keywords: *Calcium-Silicate-Hydrate (C-S-H), Microstructure, Diffusion, Long-Term Performance, Modeling*

1. INTRODUCTION

Water is an inherent constituent of concrete necessary for transforming anhydrous clinker into a solid binder connecting the aggregate. Excess water from the hydration process is later free to evaporate under ambient conditions during the structure's service life. As the water leaves the porous system, compression stresses arise in the microstructure and, due to the inhomogeneity of the concrete matrix, drying shrinkage cracks develop that compromise the material performance characteristics. It has been demonstrated that drying affects concrete properties on the material and structural levels [1,2], as well as alters properties of the hardened cement paste (HCP) [3–5]. Furthermore, we recently reported that the slow drying process and a specific type of reactive aggregate were the key factors responsible for the long-term strength increase in massive concrete elements [6] and, ultimately, for the formation of the rare calcium-aluminate-silicate-hydrate tobermorite mineral [7].

Due to its importance, the drying process of concrete elements has been studied since the beginning of modern concrete research. Initially, it was attempted to describe the process as analogous to heat transfer using a diffusion equation and a constant, material-dependent diffusion parameter. However, if the diffusivity was deduced at the beginning of drying, the drying kinetics was greatly overestimated at the later stages [8,9]. Furthermore, as the dimensions of the drying concrete element increased, the discrepancy between the predicted and measured results also increased. Finally, a nonlinear water diffusion model driven by the gradient of relative humidity (RH) was derived by Bažant and Najjar [10], assuming a constant gas pressure in the porous body. In parallel with the models for the drying of concrete elements, the theory of water transport in porous materials was developed [11–13], which allowed the production of modern multiphase transport codes [14–18]. Modern experimental techniques such as X-ray and neutron computed tomographies allow for real-time monitoring of the

moisture transport in the microstructure [19,20] and comparison with numerical predictions [21]. Although there is currently a robust theoretical basis for the description of moisture transport in partially saturated porous materials [22], concrete, as a cement-based material, represents a distinct type of porous medium. HCP, the binder in concrete, is primarily composed of calcium-silicate-hydrate (C-S-H), which, owing to the wide range of pores and complex pore connectivity, is still challenging to model and implement into multiphase programs. This primarily results from the colloidal nature of the C-S-H gel, which, unlike elastic porous materials, responds to the drying gradient with a permanent microstructural rearrangement.

During the hydration of HCP, different sizes of pores are formed, ranging from several nanometers to hundreds of micrometers [23–27]. The smallest pores can be observed at the atomistic scale of the C-S-H structural unit, while the larger gel and capillary pores result from the imperfect growth of the C-S-H hydration products or are occupied by water excessive for the hydration process. The interlayer distance measurements at the atomistic scale of the C-S-H structural unit reveal that the distance between the sheets changes with the RH [28]. On a larger scale, the overall characteristics of the bulk C-S-H gel alter due to drying [29], as documented by the measurements of the specific surface area by SANS/SAXS [30] and adsorption techniques [31,32]. It has been shown that the water in nanoscale interlayer pores can be easily exchanged to micrometer scale gel pores [33], as they are divided by movable calcium-silicate sheets [34]. Furthermore, short- and long-term measurements of desorption isotherms or drying shrinkage give different relationships between the RH and water content or drying shrinkage strain, respectively [35], which resembles other rheological behaviors of HCP. A possible explanation for these phenomena may lie in a better understanding of the mechanism in which the bulk C-S-H gel responds to the imposed drying gradients.

In recent years, several researchers have reported so-called anomalous or non-Fickian kinetics in the drying process in cementitious materials [36–38], which addresses the non-linear

proportionality of the decrease in water content to the square root of the drying time as predicted by the diffusion equation, which is currently recommended for moisture transport evaluations [39]. Typically, for the anomalous behavior, the drying samples first reach a near-equilibrium state with the kinetics obeying the square root proportionality described above; however, the mass of the drying sample continues to decrease, although with a much lower rate as compared to the initial phase. The proton NMR technique can capture the ongoing changes in the pore structure of a drying sample, and through continuous measurements of porosity during drying, it has been proposed that the changing pore structure affects the apparent water diffusivity, which results in the anomalous drying kinetics [40]. Similar to drying, the anomalous kinetics can be observed during the rewetting of severely-dried concrete samples, where this mechanism is attributable to initial water suction into drying-induced microcracks, which later act as reservoirs for water absorption into the cement paste adjacent to the microcracks [41]. To numerically model the anomalous water transport, the use of a time-dependent water permeability coefficient has been proposed [42], in addition to describing the absorption kinetics with two constant sorptivities [41] or using the so-called dual permeability model, which considers the concrete as a dual medium with two interconnected transport processes [43]. Despite the recent advancements in modeling, further research is required to improve the understanding of the underlying mechanism of the anomalous moisture behavior at the material scale and how it relates to the moisture transport characteristics.

This study summarizes water desorption isotherm data measured by various techniques over different time spans to formulate a unified water desorption model. This model is then implemented into a numerical code based on a multiphase water transport model to discuss the mechanism for the anomalous drying kinetics of cementitious materials.

2. DESORPTION ISOTHERM OF HARDENED CEMENT PASTE

2 . 1. Material and methods

A desorption isotherm provides a link between the water content and equilibrium RH at a constant temperature. Generally, the water content at a given water vapor pressure depends on the surface chemistry of the material and the characteristics of its porous system, such as pore size distribution (PSD) and pore connectivity. For cementitious materials, the sorption isotherm can be experimentally obtained by several techniques, which differ based on the measured variable and the duration of the experiment. Therefore, before proceeding to the formulation of the proposed desorption isotherm model, the reader is provided with a brief review of different desorption isotherm measuring methods, as a detailed understanding of the techniques is essential for the correct interpretation of the results. The experimental data are primarily taken from several references previously published by Maruyama and the colleagues [3,44–46]. It should be noted that the data is all from the same casting batch of cement paste; however, different techniques and sample pre-conditioning were adopted in the measurement protocols. Furthermore, the characteristic sample size used for each experiment is larger than the largest pore size intrinsic to the material, which, in the case of HCP, are the capillary pores of size in the order of micrometers [47].

Typically, in the literature, the desorption isotherm is measured by subjecting block samples to several RHs while periodically measuring the sample's mass. Once the mass reaches an equilibrium with respect to time, the water content is determined gravimetrically, and the water content is calculated using the reference dry state. In the field of cementitious materials, the reference dry state is commonly considered as the oven-dried state at 105 °C [3,38,48] or

alternatively at 20 °C through equilibration above silica gel [49], vacuum-drying, or P-drying [25,50]. The duration of the experiment depends on the thickness of the specimen; however, due to the low permeability of cementitious materials, several months or more are generally required to equilibrate the samples.

The entire measurement procedure can be made automatic if a thermogravimeter is coupled with a RH generator (RH-TG). In literature, this method is also often referred to as the dynamic vapor sorption (DVS) technique. In this case, the mass of the sample is continuously recorded, and the imposed RH can be adjusted based on the elapsed experimental time or based on the pre-defined equilibrium criterion. To shorten the time required for the technique, a thin block sample of the order of a few millimeters or sample powder is often used for the test [45], and the sorption isotherm data can be obtained within several days or weeks. On the adsorption branch, the measurement data from the DVS technique were compared with the results obtained by the traditional method and it was concluded that both methods are comparable in the low RH range; however, a discrepancy was observed above 75 % RH, probably due to insufficient equilibration time [51].

Beyond gravimetric methods, the relation between water content and RH (here more precisely referred to as the relative pressure of water vapor) can be obtained by the so-called volumetric method. A pulverized sample is placed into a system of a known volume, where, at first, the adsorption branch is measured by gradually increasing the water vapor pressure followed by a gradual desorption process. It should be noted that the air is removed from the measurement cell at the beginning of the analysis (producing a vacuum), and therefore, the water vapor pressure equals the total gas pressure in the system. Knowing the volume and analysis temperature, and measuring the water vapor pressure (therefore, the technique is sometimes referred to as the manometric method), the water content can be calculated from the ideal gas equation. This approach has its origin in adsorption analyses, where the obtained results are

151 further used to determine characteristics of the porous space in terms of the specific surface
152 area (SSA) or PSD. The merit of this method lies in the duration of the entire experiment, as a
153 pulverized sample equilibrates rapidly, and a single measurement can be typically taken within
154 several hours. As has been previously demonstrated for the SSA [3,5], this approach is suitable
155 for studying the drying-induced changes in the colloidal nature of the C-S-H gel. Furthermore,
156 accurate water vapor pressure control allows the obtainment of precise and high-resolution data.
157 However, the drawback of this method is that a dry sample is required at the beginning of each
158 analysis, which inevitably induces microstructural changes associated with the first (virgin)
159 drying at the HCP scale.

160 The results presented here are for HCP samples, which were prepared seven years ago using
161 Japanese white Portland cement with a water-cement ratio (w/c) of 0.55 (W55). The cement
162 was mixed in a pan-type mixer and then further remixed to reduce the bleeding during the
163 dormant period. The cement was cast into 3-mm-thick molds and into molds of a larger volume
164 to obtain a sufficient quantity of bulk hardened paste. The fresh paste was cured in the sealed
165 condition for four days, and then de-molded and further cured in lime-saturated water. The
166 curing took place at a controlled temperature of 20 ± 1 °C. At the age of 180 days, the 3-mm-
167 thick samples were placed into chambers with controlled RHs of 11, 20, 30, 40, 50, 60, 70, 80,
168 90, and 95 % at a temperature of 20 ± 1 °C. The desired RH was achieved using saturated salt
169 solutions. The equilibration for each RH took 12 months, after which the water content was
170 measured using the oven-dried technique. This set of samples is hereafter referred to as the
171 slowly-dried samples (SDS), and the water contents of those samples give the long-term
172 desorption isotherm by gravimetric method (L-T (g)) [3]. Apart from the data of samples
173 equilibrated for one year, we show measurements of water content after 6 months of drying for
174 the same samples.

The SDS equilibrated at each RH were subjected to short-term sorption measurements by the volumetric method (S-T (v)) after six years of equilibration. These results are nearly-equivalent to the data published previously by Maruyama et al. [3]; however, the pre-treatment procedure was slightly adjusted to obtain a more accurate relationship between RH and evaporable water for the use in moisture transport modeling. As mentioned previously, the volumetric method requires a dry sample at the beginning of the measurement. For the previous data set [3], the pre-drying was achieved by vacuum drying the pulverized samples at an elevated temperature of 105 °C. However, not only evaporable water is removed from the sample at this temperature, but also some chemically bound water related to ettringite. In the cement system, one mole of ettringite binds 32 water molecules; however, if the sample is dried at an elevated temperature, the number of moles of water is reduced to approximately 10 – 13 [52]. These water molecules are re-saturated at approximately 60 % RH during measurement of the adsorption branch of the sorption isotherm, thus slightly affecting the results. Therefore, the pre-drying procedure adopted in this study is based on vacuum drying at the ambient temperature in the experimental room (20 – 25 °C).

Finally, as the microstructure of SDS corresponds to the state obtained after six years of equilibration of the HCP at different RHs, the long-term volumetric (L-T(v)) desorption isotherm can be constructed using the rapid volumetric measurement and reading the water content at the relative pressure corresponding to the RH at which the sample was equilibrated. Such an approach will be further discussed later in this study.

It should be noted that all the isotherm data reviewed in this study were obtained after the equilibration criterion was met at the RH conditions or the drying kinetics became indetectable using the instrumentation. For the long-term data [3], this was achieved by monitoring the mass of the samples and measuring the SSA. For the short-term gravimetric data from [45], the step-by-step desorption duration was determined based on a preliminary experiment. Finally, for the

volumetric data, the equilibrium was checked based on the water vapor pressure variation in the measurement cell.

2 . 2. Short-term isotherm results on SDS equilibrated for six years

The short-term sorption isotherms for the SDS as measured by the volumetric method are shown in Fig. 1. As for the previous data [3,5], the change of the isotherm shape clearly indicates the long-term rearrangement of the microstructure of the HCP due to prolonged drying. Two features can be observed in the results from the saturated sample (W55-sat) to the sample equilibrated at 50 % RH (SDS50). First, a continuous decrease in the maximum water sorption content can be observed from W55-sat to SDS50 from approximately 300 to 200 mg/g-dry HCP. Second, a gradual shrinking of the high RH sorption hysteresis (i.e., the difference in water content at the adsorption and desorption branch above the cavitation point) is observed, proportional to the decrease in the cavitation water at approximately 35 % RH. The amount of cavitating water for the sample with a microstructure unaffected by long-tern drying (W55-sat) was approximately 25.5 mg/g-dry HCP, lowering to 9.4 mg/g-dry HCP for the sample equilibrated at 50 % RH (SDS50).

For SDS40 – 11, the high RH hysteresis and the amount of cavitating water gradually increased back up to 29.4 mg/-dry HCP for SDS11. No specific trend can be seen for the maximum water sorption content in this equilibration range as it oscillates around approximately 230 mg/g-dry HCP. The results shown in Fig. 1 were used for the development of the desorption isotherm model, as demonstrated later.

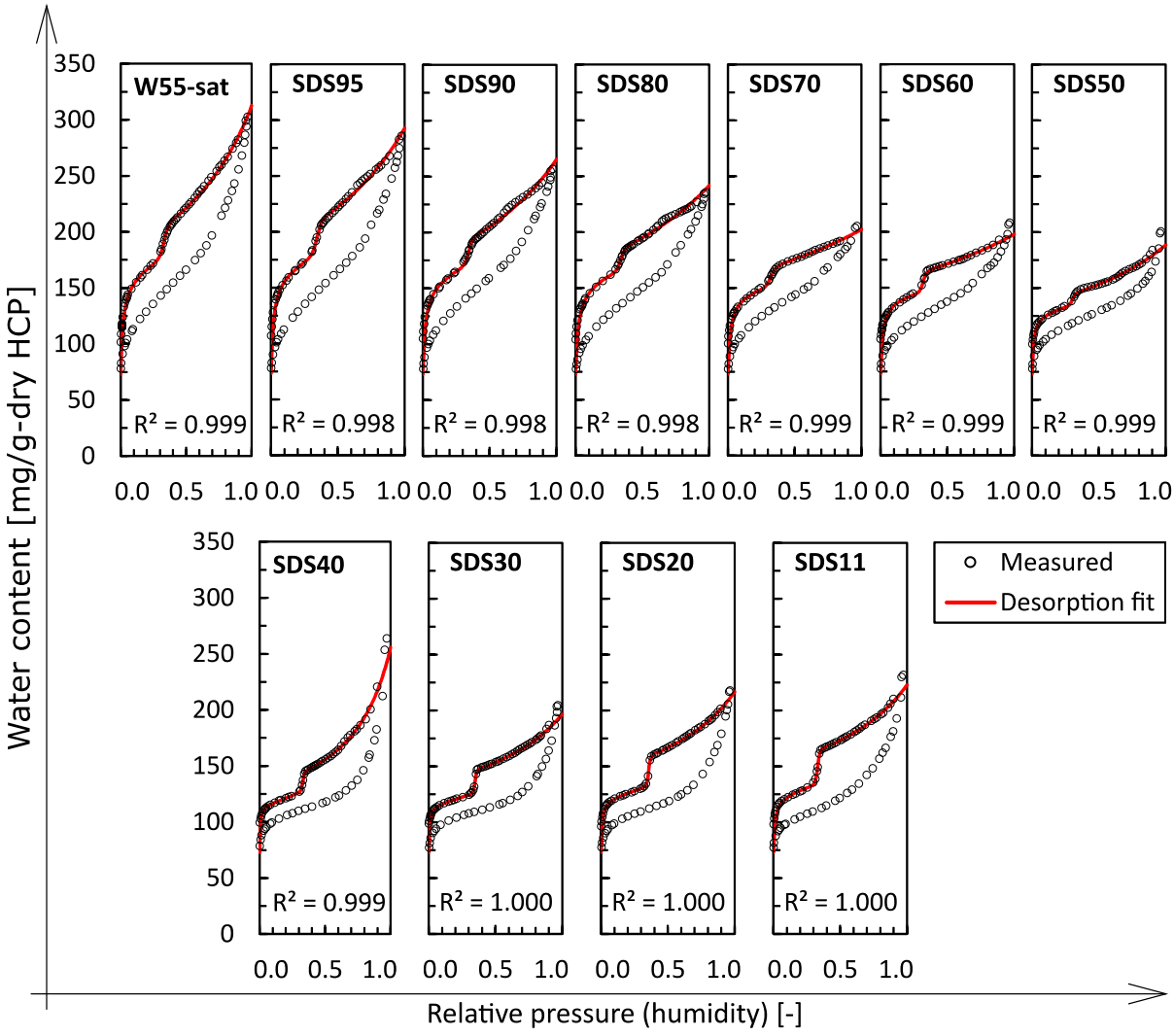

Fig. 1 Water vapor sorption isotherms measured by the volumetric method using the slowly-dried samples equilibrated at various relative humidities for six years. Both the maximum water content and the high RH range sorption hysteresis (i.e., the difference in the adsorption and desorption branch above approximately 0.35 relative pressure) decrease from the saturated state to the sample equilibrated at 50 % RH. For the samples equilibrated at 40 – 11 % RH, the high range sorption hysteresis is regained. The red line is the fit of the experimental data using the extended Guggenheim-Andersen-de Boer (GAB) given by Eq. (1). The results of the fitting are plotted in Fig. 4.

2 . 3. Comparison of the short-term desorption isotherms

The experimental results, which span from hours to a few days, are compared in this section.

Fig. 2 compares the sorption isotherm obtained by gradual drying of a 1-mm-thick sample in

[46] (gravimetric method) with the isotherm for sample W55-sat as measured by the volumetric method. Due to the rapidity of the test, it is assumed that the relationship between water content and RH is minimally affected by the colloidal nature of C-S-H in both cases. More precisely, the microstructure of the C-S-H is not affected by the long-term drying-induced microstructural rearrangement or it occurs in a slower time scale than the measurement itself, and therefore, it cannot be seen. Therefore, we assume that during the short-term measurements, the water content over the entire range of RHs is established only from the viewpoint of thermodynamics on a porous system, which is not significantly affected by any permanent rearrangement. This assumption is supported by a preliminary experiment, which showed a decrease in SSA for repetitive measurements separated by 18.5 hours of approximately 1.5 %. Compared to the reduction of SSA due to long-term drying, which can reach up to approximately 50 % of the initial SSA [3], the rearrangement of the microstructure during the short-term measurements seems negligible.

It can be observed that while the desorption isotherms from both methods provide different relationships at high RH, this discrepancy is reduced with decreasing RH until approximately 35 %, below which both methods match. This discrepancy results from the fact that the volumetric sorption measurement starting from the dry state, and thus, initial drying is required. The first (virgin) drying induces irreversible changes at the HCP scale, which leads to a change in the sorption properties as compared to a never-dried sample. Furthermore, considering the steep increase in water content for the volumetric method at a RH above 90 % and that the sample cannot be fully re-saturated (i.e., reaching 100 % RH), the initial point of the desorption branch is shifted towards a lower water content.

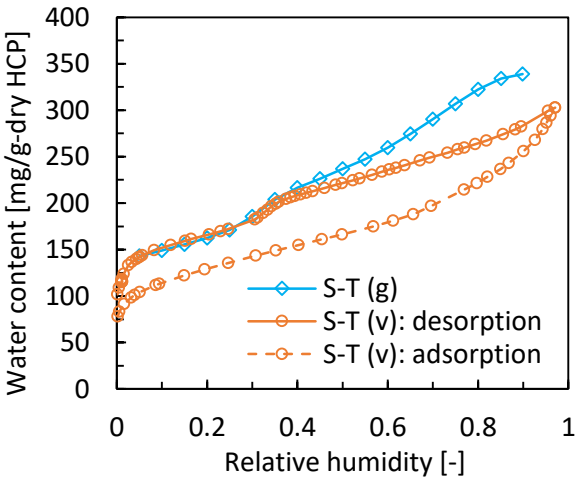

Fig. 2 Comparison of the short-term desorption isotherms obtained by the volumetric (S-T (v)) and gravimetric methods (S-T (g)). The microstructure of the C-S-H gel is assumed to remain stable during both measurements.

To account for the difference between the gravimetric and volumetric measurements shown in Fig. 2, a theoretical model was formulated to address the gap in water content due to first-drying. This first-drying (FD) model is based on a prescribed pore size distribution, which represents the volume of pores lost due to the first drying. The water content at a given RH is calculated assuming a meniscus between two layers of adsorbed water inside the cylindrical pores. This method relies on the Kelvin equation and is analogous to the procedure described in [53]. In the FD model, it is assumed that as the meniscus recedes, the pore's volume, which corresponds to the evaporated water, is inevitably lost. Furthermore, after the water evaporates from the meniscus, the water adsorbed on pore walls does not contribute to the total water content, as this water would still be captured in the experimental isotherm measured by the volumetric method. The detailed model formulation is shown in Appendix C.

2 . 4. Long-term desorption isotherm

In Fig. 3 (left), the short-term isotherm measured by the gravimetric method is compared with the long-term isotherms from [3], which was measured after one year of equilibration. For comparison, also the desorption isotherms after six months and six years of equilibration are plotted in Fig. 3 (left). The six-year data were obtained from the volumetric measurements as will be described later.

As has been previously reported in [3], looking at Fig. 3 (left), it can be observed that the long-term measurements by the gravimetric method give significantly lower water content than the short-term results. During the drying, the discrepancy begins at approximately 90 % RH and continues through the remaining desorption range; however, from approximately 35 % to 11 % RH, the gap between the short-term and long-term data is somehow reduced.

Comparing the six-month and one-year gravimetric data in Fig. 3 (left), it is evident how the water content continuously decreases as the drying time is prolonged. Owing to the sample's thickness of 13 mm, the six-month drying provides enough time for the internal RH to equilibrate with the external environment. Later in this paper, it will be shown based on numerical simulations that the internal RH equilibration is achieved within several weeks of drying. Therefore, the continuous reduction of the equilibrium water content from six months to one/six years can be attributed to the drying-induced microstructural rearrangement, which can be observed on the months/years time scale. A small discrepancy can be observed in the six-month data at 11 % and 20 % RH, which show slightly lower water contents than the one-year drying data; however, the overall trend suggests that this may originate from some experimental inaccuracy.

As the water content in the porous material at a given RH depends on the sample's microstructural characteristics, such as pore size distribution, the discrepancy between the data can be explained by a long-term microstructural rearrangement. For instance, this mechanism

was documented in [3] through water vapor measurements of the SSA, which reduced by approximately 50 % between the saturated and 40 % RH conditions. The same conclusion can be drawn if the SSA is measured by nitrogen gas, although the SSA quantitatively differs when measured by these two probing substances.

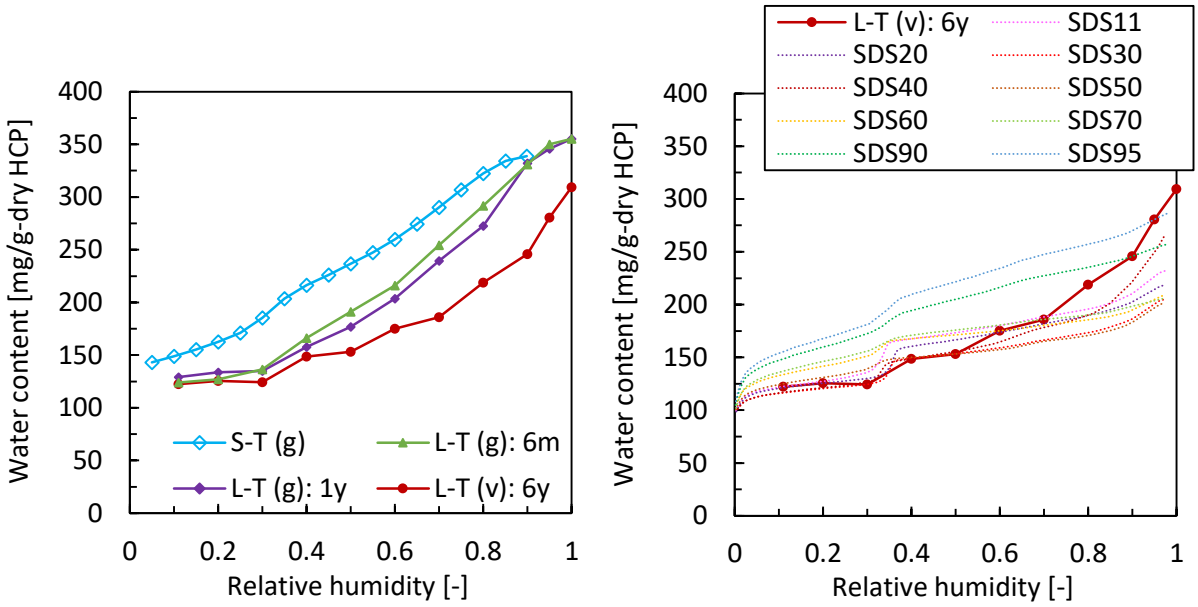

Fig. 3 (left) Summary of the desorption isotherms as measured by the short-term (S-T) gravimetric method (g) and the long-term (L-T) gravimetric and volumetric methods (v). The long-term drying data are given at six months (6m), one year (1y), and, in the case of the volumetric measurements, six years (6y). (right) The long-term desorption isotherm obtained from the volumetric method data of samples equilibrated for six years at different relative humidities. The short-term volumetric measurements of the slowly-dried sample (SDS) from Fig. 1 are shown by the dotted lines to illustrate the construction of the long-term volumetric isotherm.

Similar to the short-term measurements, long-term (de)sorption isotherms can be obtained both gravimetrically and volumetrically, as shown in Fig. 3 (right). The long-term volumetric desorption isotherm was obtained using the SDS results shown in Fig. 1 by reading the water content at the relative pressure corresponding to the respective long-term equilibration RH. From this perspective, the equilibrium water content is established considering both the thermodynamics and the microstructural rearrangement. The long-term desorption isotherms

by the volumetric and gravimetric methods show a similar trend when compared in the low RH range from approximately 11 – 40 % RH, while the discrepancy increases at the higher RHs. Again, the lower water contents measured by the volumetric method can be explained by the combination of irreversible changes in the microstructure on the HCP scale associated with the first drying and incomplete saturation of the sample during the adsorption branch measurement. Furthermore, it can be observed that in the low RH range of 11 – 40 %, the water content after six years of SDS equilibration is lower than the original results from [3], which were obtained after one year of equilibration. Considering that the thickness of the samples was just 13 mm, this suggests a rearrangement on the scale of the C-S-H gel occurring on the time scale of several years.

2 . 5. Desorption isotherm model

For numerical modeling, the sorption isotherm is often described using adsorption theory. Similarly, as for the other porous materials, the Brunauer-Emmett-Teller (BET) method is applicable for HCP for a RH between 5 % and 35 %. The Guggenheim-Andersen-de Boer (GAB) method was proposed to extend the fit of the isotherm data to almost all RHs [54,55]. Unlike other relationships for capturing the sorption isotherm data summarized for instance here [56], the parameters of the BET and GAB models can be derived based on the adsorption theory and have physical meanings [57]. Both BET and GAB equations have been widely used to describe the microstructure of cementitious materials in terms of the SSA. This is done by evaluating the amount of water content that is adsorbed on a dry sample, for which, naturally, the adsorption branch of the sorption isotherm is used. However, as this study aims to numerically model the drying of HCP, the desorption branch is the primary concern. For this

purpose, the sudden drop in water content (also referred to as the kink on the desorption isotherm) was necessary to consider, which occurs at approximately 35 % RH at 20 °C. Using the short-term sorption measurements, this rapid loss of water within a narrow range of RH was attributed to the cavitation of the water condensed inside the gel pores of the C-S-H gel surrounded by narrow necking interlayer spaces [44]. According to the traditional tensile strength hypothesis [58], cavitation occurs during desorption when the decreasing RH imposes negative pressure on the liquid phase (as can be calculated by the Kelvin equation) stretching the condensed water beyond its ultimate tensile strength. If the size of the necking pore is smaller than a given threshold value, the tensile strength of water is reached before the evaporation of water molecules from the receding meniscus, and a metastable rupture develops in the liquid phase leading to the sudden evaporation of the entire volume of condensed water.

To account for the cavitation mechanism, the GAB equation was extended with the activation term using the logistic function. The extended GAB equation is given as

$$w = \frac{C\ k\ w_m\ h}{(1 - k\ h)[1 + (C - 1)k\ h]} + \frac{L_k}{1 + e^{-s_k(h - h_k)}}\ , \tag{1}$$

where w and w_m are the water content [mg/g-dry HCP] and the monolayer water content [mg/g-dry HCP], respectively, C and k are the monolayer and multilayer energy constants [-], respectively, h is the relative pressure/humidity [-], L_k is the amount of cavitating water [mg/g-dry HCP], s_k is the slope of the cavitation drop [-], which describes how well the cavitation is localized on the desorption isotherm, and h_k is the RH of the cavitation midpoint [-].

As shown in Fig. 1, Eq. (1) can closely describe the experimental data of the short-term desorption isotherms. The dependency of the parameters of the extended GAB equation on the RH of the long-term equilibration is shown in Fig. 4 together with the fitting functions used for numerical modeling.

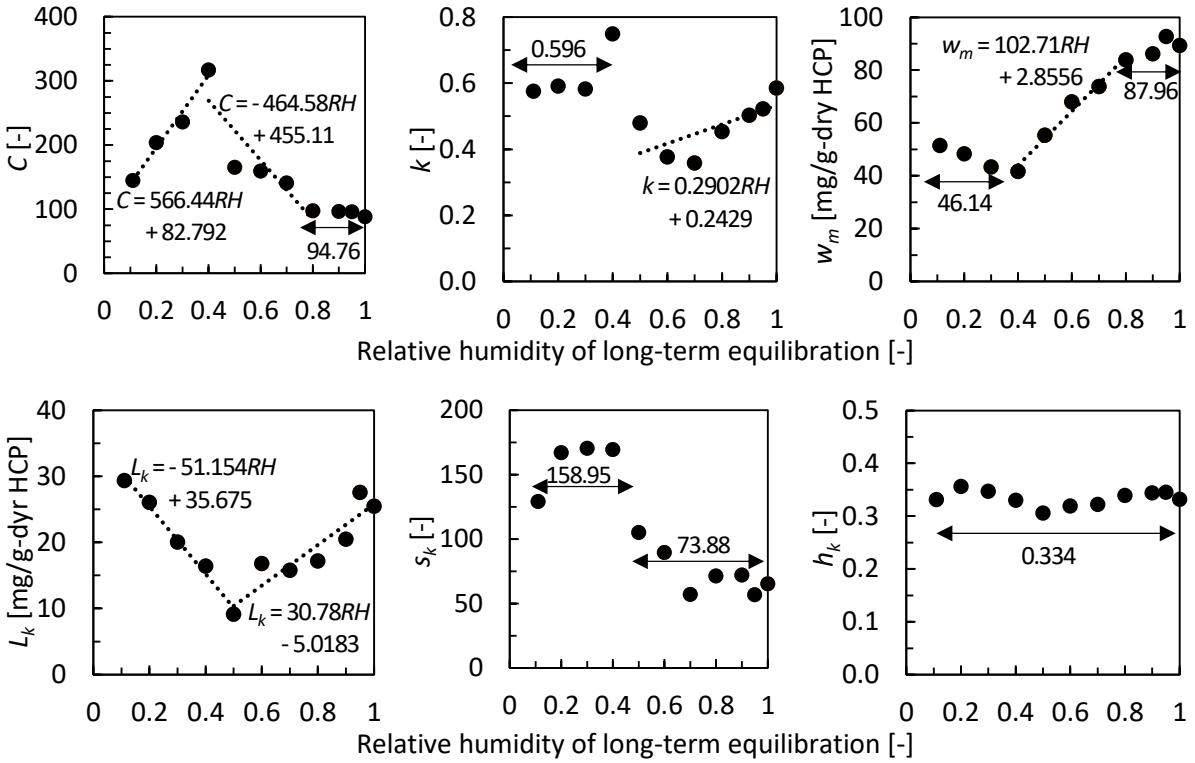

370 *Fig. 4 Parameters of the extended GAB equation, Eq. (1), obtained from the short-term volumetric*
371 *data shown in Fig. 1.*

372

373 **2 . 6. Modeling of the microstructural rearrangement**

374

375 In the previous section, the experimental results were used to demonstrate how the long-term
376 drying-induced microstructural changes result in a shift of the desorption isotherm towards
377 lower water content at a given RH. To complete the model, the kinetics, in which this change
378 occurs, must be formulated. Based on Fig. 3 (left), the water content at a given RH depends on
379 both the thermodynamic equilibrium and its duration. An analogy can be found with mechanical
380 systems, where the load-induced strain increases even after the initial material deformation.
381 Concrete under general loading conditions transfers the stress through elasto-visco-plastic
382 strain, while at the macroscopic scale, the viscous strain dominates the long-term strains [59,60].
383 The visco-elastic behavior originates from the HCP and can be assessed by small-scale
384 techniques at the nano/microscale scale of the material [61–63]. It is plausible to assume that

385 the stresses (or their variation from the initial state) generated by water during drying would be
386 transferred similarly as the stresses caused by mechanical loads, and that they would thus result
387 in an instantaneous and viscous response. Therefore, during the course of the drying, the
388 microstructure alteration is time-dependent due to water-induced stresses rather than occurring
389 concurrently with decreasing water content. The total equilibrium at a given RH thus depends
390 on both the thermodynamic equilibrium and the microstructural rearrangement equilibrium,
391 meaning that the water content depends on the RH and the current state of the still-evolving
392 microstructure. In other words, by the term microstructural rearrangement, we refer to the
393 permanent changes in the microstructure induced by the long-term drying and not the
394 instantaneous strain induced by the presence of water in the porous body, which deforms the
395 microstructure elastically.

396 It is assumed that the microstructure rearranges due to the creep induced by the forces related
397 to the presence of water in the porous body. Thus, the change in the water content is treated as
398 a time-dependent process as

$$w(t) = w_0 + \alpha \ln\left(1 + \frac{t}{\tau}\right) \quad , \tag{2}$$

399 where $w_0(h)$ is the initial water content [g], $\alpha(h)$ is the RH-dependent microstructure
400 rearrangement factor [g], t is the drying time [s], and τ is the characteristic time [s].
401 A similar function was previously used to describe the kinetics of the creep of cementitious
402 materials [62,64,65]. To explore if the long-term microstructural rearrangement originates from
403 the stresses acting on C-S-H gel due to water-related forces, we adopted the kinetics given by
404 Eq. (2) to reduce the water content over the drying time. This is realized through the transition
405 of the short-term desorption isotherm into the long-term desorption isotherm.

406 The logarithmic decrease of water content with the drying time is suggested by the raw data
407 from the volumetric measurement method. During the measurement of the desorption branch,

the water vapor pressure is step-by-step decreased to remove the water molecules from the sample and equilibrate it at different water vapor pressures. In Fig. 5, the raw data of equilibration at target relative pressure of 0.66 is shown. Although that the equilibration criterion set as 0.05 torr/min was met, when plotting the data in the logarithmic scale a slow increase following the kinetics suggested by Eq. (2) can be observed at the second half of the equilibration period. This increase in the measured water vapor pressure indicates that further water molecules are removed from the sample thus reducing its water content.

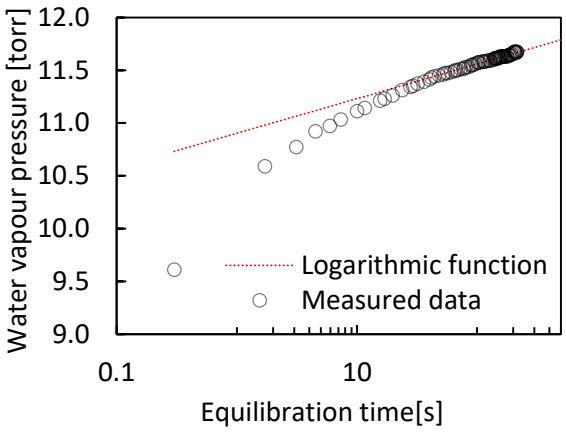

Fig. 5 Logarithmic equilibration kinetics observed during a measurement by the volumetric method at target relative pressure of water vapor of 0.66. A logarithmic function plotted in red is prescribed by $p=p_0+\alpha \ln(t/\tau)$.

As a first approximation, the parameter τ in Eq. (2) was estimated using the data shown in Fig. 3 in the range from 11 – 40 % RH, where these results correspond to ages of 3.7 – 5.7 hours, six or twelve months, and six years for the short-term volumetric, long-term gravimetric, and long-term volumetric data, respectively. For the short-term volumetric data, the beginning of the desorption branch of the measurement was considered as the beginning of the drying process.

Since the objective here is to capture the behavior on the level of C-S-H gel, the fitting was conducted in the low RH to minimize the impact of water in larger pores. Fig. 6 (left) shows the low RH range, where the fitting was conducted with the measured and fitted data. In Fig. 6 (right), the decrease of the water content at given RHs is shown together with the fitting functions. The parameters of the fit were $w_0(h)$, $\alpha(h)$, and τ. The characteristic time yielded the final value τ = 3.35 hr. It is important to point out that considering the drying time even for the short-term desorption data, the impact of the permanent microstructural rearrangement, which develops during the short-term measurement, was considered in the fitting of τ.

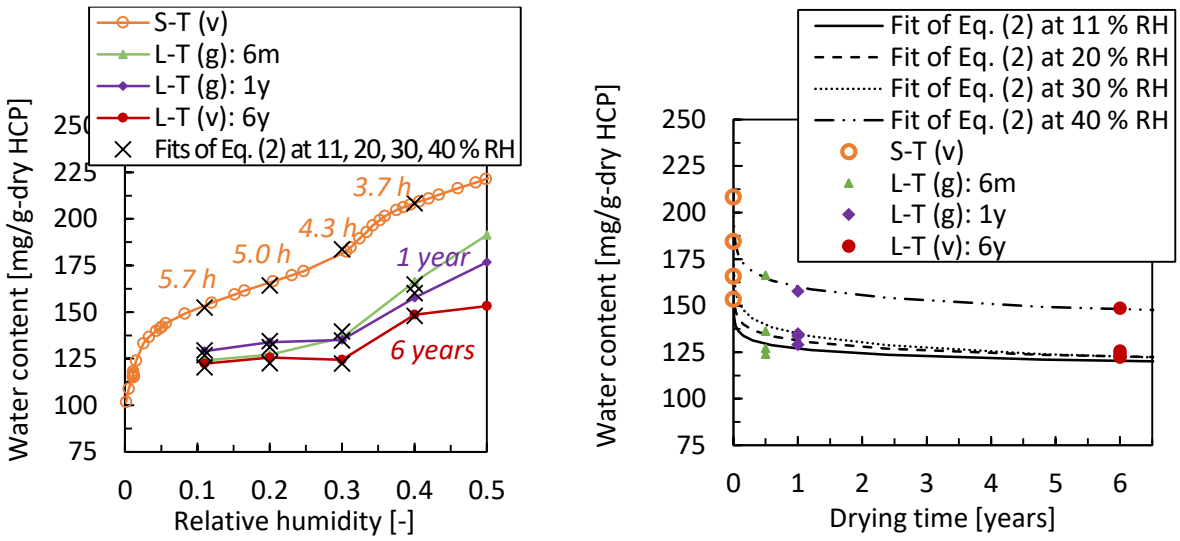

Fig. 6 (left) Details of the fitting of Eq. (2) to the available experimental data. The continuous lines represent the desorption isotherm data from Fig. 3 and the "x" markers represent fit results at relative humidities of 0.11, 0.20, 0.30, 0.40 for the short-term desorption isotherm and for drying times of six months (6m), one year (1y), and six years (6y). (right) The continuous line represents the fits of Eq. (2) and the scatter data points are the water contents at different relative humidities.

2 . 7. Desorption measurements summary

Before proceeding to the implementation of the desorption model into a numerical model, the main findings of the experimental section are briefly summarized.

First, in Fig. 1, the short-term sorption isotherms on the samples equilibrated for the 6 years at different RH conditions are shown. From the saturated sample (W55-sat) to the sample equilibrated at 50 % RH (SDS50), the total water content, high RH hysteresis, and the amount of cavitating water gradually decrease. This suggests a reduction in the mesopore volume on the scale of C-S-H gel. For the samples dried at RH below 40 % (SDS40 – SDS11), the amount of cavitating water and the high RH hysteresis increase, and the measured isotherms show no specific trends. For the fitting of the desorption branch of each isotherm, the extended GAB equation is proposed with an activation term accounting for the cavitating water. The results of the fitting to the extended GAB equation are given in Fig. 4.

The data measured by the volumetric method were compared with the results of the gravimetric method. As shown in Fig. 2, in the low RH below the cavitation point, both methods give the same results, however, in high RH range, the gravimetric methods give larger water content at given RH since some pore volume on the level of HCP is irreversibly lost during the pre-drying required for the measurements by the volumetric method.

As shown in Fig. 3 (left), comparing the desorption isotherm data measured in the time scale of hours/days with the data measured in the time scale of months/years, it is shown how the water content is reduced due to long-term equilibration at constant RH conditions. It is hypothesized that this long-term decrease in water content is related to creep induced by the water-related forces, which affects the microstructure of the C-S-H gel. Assuming that the long-term decrease in water content is related to the creep of the C-S-H gel, a logarithmic kinetic was chosen to capture it. The logarithmic kinetics is also indicated by the raw equilibration data from the volumetrics measurements shown in Fig. 5.

The desorption data are summarized in Fig. 3 (left) for short-term desorption isotherm by the gravimetric method and the long-term desorption isotherms for drying times of six months, one year, and six years.

3. NUMERICAL RESULTS

3 . 1. Numerical model description

The sorption isotherm model was implemented into a numerical code for multiphase moisture transport, where the concrete is composed of solid, liquid, and gas phases. The gas phase is a binary mixture of dry air and water vapor, referred to together as wet air. Under pressure gradients, the liquid phase and wet air are transported by advection obeying Darcy's law, while the water vapor within the wet air moves from the region with more water molecules to the region with fewer water molecules driven by the diffusion mechanism following Fick's law [22]. The derivation of the transport equations and the numerical solution using the finite difference method is explained in more detail in Appendix A and B, respectively.

Before presenting the results of numerical validation of the desorption isotherm model, the parameters used for the numerical modeling in Section 3 are given. The intrinsic permeability was taken as $1 \cdot 10^{-21}$ m^2 [66], and for the relative permeabilities of the gas and liquid phases, the van Genuchten model [13] was used with a β parameter of 2.1684 [66]. For the numerical simulation of the concrete drying, it was assumed that the process is controlled by the HCP, and therefore, the same parameters were used.

The model was validated against the drying data of HCP and concrete given by Baroghel-Bouny [49], short-term [45] and long-term (i.e., SDS samples) [32] drying data of white cement paste W55 used in this paper, and the data given by de Burgh and Foster, which exhibit anomalous drying kinetics [38]. The material characteristics used for the simulation of each experimental result given in Section 3 are summarized in Table 1. The time step was varied during the

calculations to obtain optimum calculation speed while maintaining the convergence of the solution. For modeling of the drying process of the larger samples used in the experiment by Baroghel-Bouny, the maximum time step was approximately 15 minutes while, for the thin samples used in other experiments, the time step was generally in the range from 3 to 12 seconds.

Table 1 Summary of the material characteristics used for validation of the numerical code.

experimental data	Baroghel-Bouny [49] (HCP / concrete)	W55: short-term [45]	W55: long-term (SDS) [32]	de Burgh and Foster [38]
thickness [mm]	100	1	3	varying between 3 – 4
initial RH [%]	87 / 93	97	97	98
drying RH [%]	50	gradual 90 – 15	varying between 95 – 11	varying between 93 – 11
temperature [°C]	20	20	20	23
porosity [%]	30.3 / 12.2	50.4	50.4	39.0
boundary node spacing [mm]	19.0	1.0	3.0	0.2

3 . 2. Experiment by Boroghel-Bouny

Several numerical models [66–68] were validated against the data from Baroghel-Bouny [49]. In the experiment, the cylindrical HCP (CO) and concrete (BO) samples were cured in a sealed condition for two years prior to one-dimensional drying at 20 °C and 50 % RH. Fig. 7 compares the numerical and experimental results of the relative weight loss with respect to the initial mass during the drying process. These results demonstrate the general capability of the moisture

transport code combined with the sorption isotherm model to predict the drying of cementitious materials.

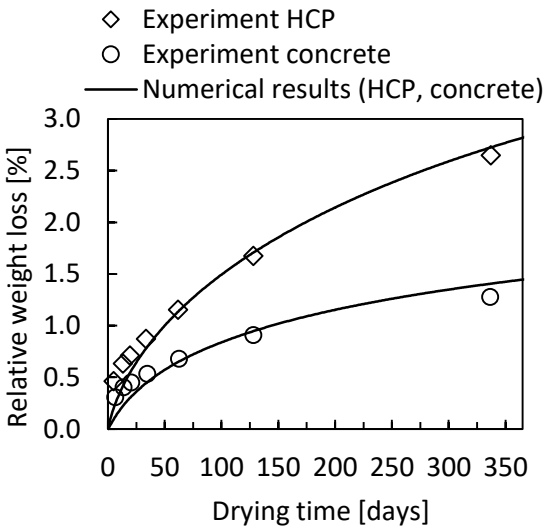

Fig. 7 Results of the validation of the numerical model against the experimental results from Baroghel-Bouny [49] *for hardened cement paste (HCP) and concrete samples.*

3 . 3. Reproducing the short-term and long-term experimental results

Second, the numerical code was validated by reproducing the experimental data used for the formulation of the desorption isotherm model. It should be noted that the experimental set-up has an impact on the boundary conditions of each experiment. For example, forced drying in a dynamic water vapor analyzer, where a mixture of nitrogen and water vapor is directly blown on the sample, results in a steeper RH gradient at the sample's boundary as compared to drying above a saturated salt solution, where the surrounding air is quiescent. As Neumann boundary conditions were implemented, where the flux through the boundary depends on the spacing of the fictitious boundary node, this spacing was adjusted based on each experiment to fit the initial slope of the mass loss curve.

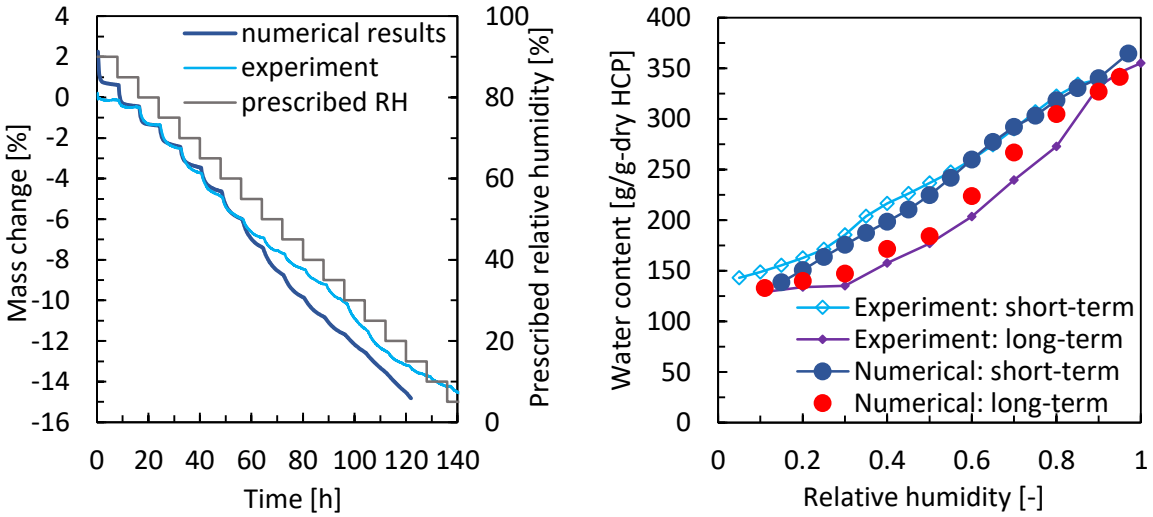

529 *Fig. 8 Validation of the numerical code against the experimental data from the short- and long-term*
530 *experiments.*

531

532 The short-term gravimetric experiment consisted of drying a 1-mm-thick sample subjected to a
533 decreasing RH from 95 % to 20 % RH in increments of 5 % every eight hours. The calculated
534 mass change of the sample during the short-term experiment is compared with the measured
535 data in Fig. 8 (left), and the experimental and numerical desorption isotherms are compared in
536 Fig. 8 (right) for both the short- and long-term drying experiments. It should be noted that the
537 short-term experiment is sensitive to the boundary conditions, and as the spacing of the
538 fictitious node was fitted at a high RH, its value may differ at low RH. Furthermore, the problem
539 was simplified as a 1D problem, although the actual sample has dimensions of 3 x 3 x 1 mm.
540 Regardless of these shortcomings in the numerical modeling, the obtained short-term
541 desorption isotherm agrees well with the experimental data mainly in the high RH range.

542 To reproduce the long-term experiment, the drying of a 3-mm-thick sample at different RHs
543 for one year was simulated. As compared to the short-term drying, the additional decrease in
544 the water content is captured by the numerical calculations. Although a slight discrepancy
545 between the numerical and experimental data can be observed, especially for a RH between 60
546 – 80 %, the results show additional water loss as compared to the short-term results. Importantly,

547 the long-term validation demonstrates the general ability of the model to capture correctly the
548 moisture transport of the material with the delayed microstructural rearrangement.
549
550 **3 . 4. Experiment by de Burgh and Foster**
551
552 A high-resolution data set showing the anomalous sorption kinetics was published by de Burgh
553 and Foster [38]. The HCP samples were mixed with a w/c of 0.45 and cured in the sealed
554 condition for more than 170 days before the desorption experiment. The mass of thin discs with
555 a thickness of approximately 3 – 4 mm was frequently measured during drying inside boxes
556 with various controlled RHs for more than 40 days. For the numerical calculations, the basic
557 data set measured at 23 °C was selected, which, especially in the range from 33 – 58 % RH,
558 demonstrates the anomalous desorption kinetics.
559 The numerical and experimental results are compared in Fig. 9. Quantitatively, for multiple
560 RHs, it can be observed that the numerical results tend to approach slightly different
561 equilibriums than those obtained experimentally. This may be explained by the proposed model
562 being developed based on the data from HCP with a higher w/c and using samples with different
563 curing conditions, as the microstructure of sealed-cured samples can be already affected by
564 drying due to the self-desiccation. In contrast, the qualitative comparison of the numerical and
565 experimental equilibration kinetics exhibit similar trends, clearly demonstrating the anomalous
566 behavior for RHs of 33, 43, 58, and 75% while being less or not apparent for 11, 85, and 93 %
567 RH. In this regard, the main difference is that for the numerical results, the anomalous kinetics
568 are less apparent at 33 % RH than at 58 % RH, while the experimental results suggest the
569 opposite trend. The numerical results of the sample equilibrated at 43 % RH match the
570 experimental data well.

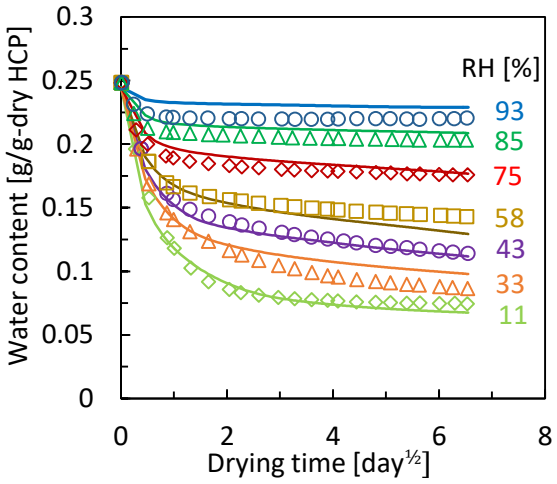

571

572

573 *Fig. 9 Numerical simulation of the drying experiment by de Burgh and Foster* [38]. *The results are for*
574 *HCP samples with w/c = 0.45 and dried at 23 °C, and show the anomalous desorption kinetics for*
575 *drying at 33 – 75 % RH.*

576

4. DISCUSSION

4 . 1. Kinetics of anomalous drying and the experimental scale

Fig. 10 shows a 3D representation of the numerically simulated one-year drying process of SDS50 in terms of saturation. The 3D surface, which represents the state of the microstructure, is reproduced based on the GAB and FD models, and a theoretical cut through the surface perpendicular to the time axis gives a theoretical, instantaneous desorption isotherm unaffected by the microstructural rearrangement at the scale of the C-S-H gel. The actual drying path, which would be measured during the experiment, is represented by the continuous line together with its projections in 2D planes as shown in dashed lines. Based on Fig. 10, it can be observed how the saturation initially rapidly decreases due to equilibration of the internal RH in the sample with the RH of the external environment. For this 13-mm-thick sample, this initial phase is completed within approximately 28 days from the beginning of the drying, during which the sample RH is lowered to approximately 51 % RH. Naturally, due to the decreasing internal RH, this period is associated with a major drop in saturation. Once the internal RH is nearly in equilibrium with the external RH, the decrease in saturation continues at a much lower rate; however, an additional decrease in saturation of 6.8 % occurs over the remaining eleven months of the experiment. As the total one-year saturation loss is 46.3 %, the additional drying after 28 days represents approximately 14.7 % of the total water loss.

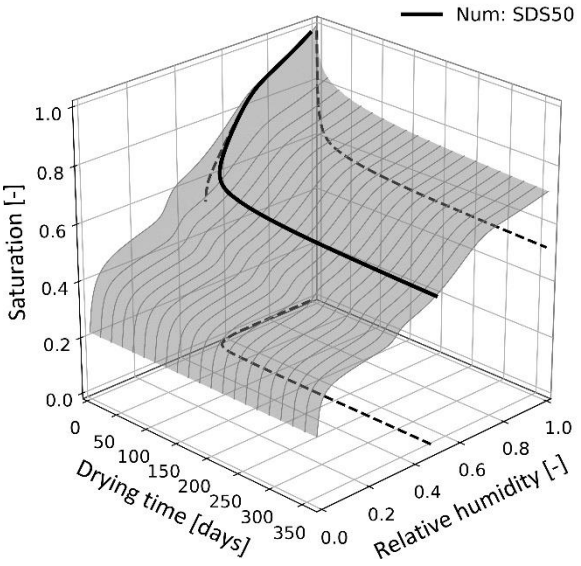

597

598

599 *Fig. 10 The numerical reproduction of the one-year drying of the slowly-dried sample at 50 % RH*
600 *(SDS50). The initial drying phase associated with the major decrease in saturation occurred within*
601 *the first 28 days; however, the continuous loss in saturation over the remainder of the simulation*
602 *accounts for the additional saturation loss of approximately 6.8 %.*

603

604 The long-term continuous loss of water was recently addressed in several studies. The mass
605 change of the drying sample not reaching equilibrium after the initial rapid drying, and the non-
606 linearity of the long-term decrease in water content with the square root of time rule as predicted
607 by the diffusion equation, are typical manifestations of the so-called anomalous or non-Fickian
608 diffusion [36]. This phenomenon has been observed in several experimental data sets [37,38],
609 which have typically aimed to rapidly obtain the desorption isotherms using small-scale
610 samples. As demonstrated in Fig. 10, for a sample with a small drying thickness, the internal
611 RH equilibrates quickly, which causes the anomalous kinetics to be observable. Alternatively,
612 if a larger specimen is used for the experiment, the initial phase of RH equilibration is long and
613 a depth-wise gradient is formed through the sample. As the kinetics of microstructural
614 rearrangement is modeled here using the logarithmic function, its rate decreases over time,
615 which would hinder the anomalous kinetics in larger specimens.

The relationship between water content and RH is crucial for many engineering applications. For example, drying causes a variation in strength at both the material [2,3,5,69] and structural scales [1]. The internal RH is important for evaluating the risk of occurrence of the alkali-silica reaction [70–72]. Furthermore, drying was recently identified as the mechanism that controls the development of long-term mechanical properties due to the feldspar-HCP reaction inside a Japanese nuclear building [6,7]. Therefore, for engineering applications, the rapid measurements on small samples may neglect the long-term decrease in water content associated with the drying-induced microstructural rearrangement, and thus do not provide a reliable relationship for evaluating the drying of actual concrete structures.

4 . 2. Mechanism of the long-term rearrangement of C-S-H gel

Many studies have suggested the rearrangement of the HCP microstructure upon drying. Furthermore, as demonstrated in the present study, the duration of the drying plays an important role, as the microstructural rearrangement is a rheological phenomenon. Little attention is given to the actual driving force, which alters the microstructure in the long-term. For a dynamic change in the desorption isotherm, the kinetics are described as analog to the creep of concrete under mechanical loads. It is well established that the creep of HCP originates from the amorphous C-S-H gel, as has been confirmed by mechanical methods such as nanoindentation [61–63]. During such experiments, the indenter’s tip generates mechanical stress, which causes instantaneous and delayed deformation. Similarly, the stress in the bulk C-S-H gel can be generated by water-related forces as the receding capillary meniscus subjects the gel to compression. In this context, the capillary forces should not be limited to acting in only the so-called capillary pores, which is the concept proposed by Powers [73] for pores related to the

volume of excess water for the hydration process, but also in smaller pores originating from the imperfect growth of the hydration products. These so-called gel pores, which can be further divided into small and large gel pores [47], are intrinsic to the growth of the C-S-H hydration products, and their width allows water condensation and the formation of a capillary meniscus.

As documented by the Kelvin equation, the compression generated by the capillary pressure increases with decreasing RH in the porous body. Recently, it has been shown that emptying of the gel pores is delayed due to narrow interlayer spaces between the sheets of C-S-H and that the gel water is evaporated through the cavitation mechanism [74]. Furthermore, the close relationship between the gel and interlayer has been observed in the exchange in water [33], which is in line with the Feldman and Sereda model [24] as well as with more recent structural models of C-S-H gel [34,75].

Considering the stress state of the bulk C-S-H gel during drying, the compression also arises from the interlayer pores. The distance between two C-S-H sheets is not constant during drying. For well-ordered C-S-H, the distance of approximately 1.40 nm between two sheets at the saturated state reduces to 1.13 nm at the dry state [28], and can be, at least partially, restored during rewetting. This process is driven by the high affinity of water molecules to the solid skeleton, which leads to the disjunction of the C-S-H layers. Once the water is removed from the interlayer space, the disjoining force is relieved, and the interlayer distance closes. In the case where several layers are stacked one after another, a compression in the bulk volume can be generated during the drying if the compression pressure is not relieved through detachment of the layers at a certain place.

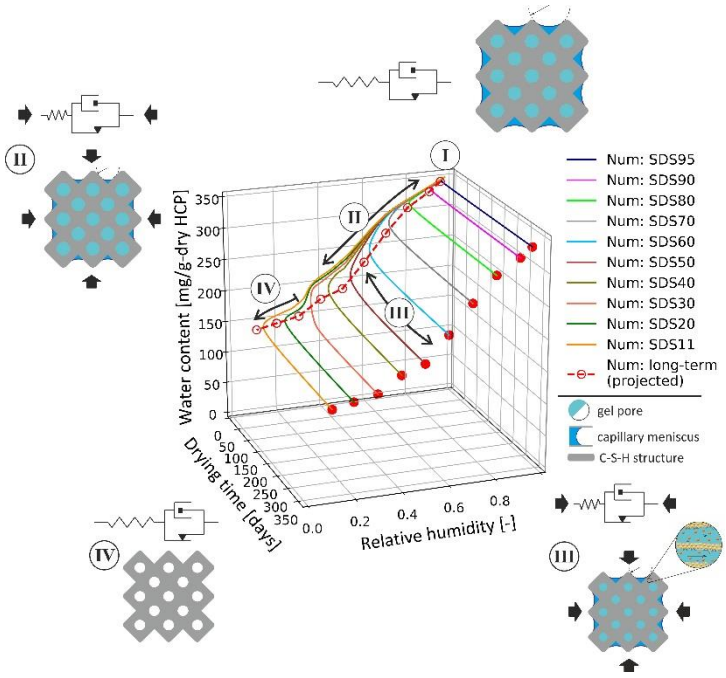

Fig. 11 Results of the numerical simulation of the drying process of the slowly-dried samples (SDS) together with a schematic representation of the state of the bulk C-S-H gel. The end of the drying process is marked with filled red circles, which are projected to the water content-RH plane.

The state of the bulk C-S-H gel is shown schematically in Fig. 11 together with the numerical results of the drying process of the SDS, where the initial state of the bulk C-S-H gel prior to drying is depicted as State *I*. Regardless of the origin of the pressure, the bulk C-S-H gel is under compression during drying, as described previously. In the short-term drying experiment, the compression of the bulk C-S-H gel results in an instantaneous deformation in both the liquid and solid phases. Neglecting the irreversible changes at the HCP scale, the bulk C-S-H gel behaves nearly elastically during the short-term drying as shown by State *II* in Fig. 11. In the long-term, if the compression stress is not relieved, the confined water leaks from the bulk C-S-H through narrow interlayer spaces. The state of the water in such narrow interlayer pores differs widely from that of bulk water since the interlayer water has much higher viscosity [76], which explains the slow rate of the microstructural rearrangement. Similar to the effects of long-term mechanical stresses, the long-term drying induces a viscous response in the bulk C-

S-H gel. Such behavior is illustrated as State *III* in Fig. 11. Furthermore, this interpretation is supported by recent studies, which have shown for well-dried samples that the layers/sheets of C-S-H behave elastically in all directions [77], which suggests that the plastic deformation associated with the drying-induced long-term microstructural rearrangement is accumulated in the volume previously occupied by the gel water. In other words, the interlayer space between the C-S-H changes due to drying, while its behavior is completely elastic and the long-term microstructural rearrangement is associated with gel pores.

In the RH range below the cavitation point, the interlayer water content is continuously reduced and the distance between the C-S-H sheets decreases [28], which increases the mechanical stiffness of the bulk C-S-H gel as has been documented by microindentation experiments [4,78]. Therefore, during drying, this increase in the stiffness stabilizes the microstructure of the bulk C-S-H gel at the low RH. This can explain the drying kinetics in Fig. 9, where the anomalous drying is apparent in the range from 33 % to 58 % RH, but is less visible for the drying at 11 % RH. From this perspective, the water content in the interlayer space governs the rate of microstructural rearrangement.

The hypothesis that the drying-induced microstructural rearrangement originates from the long-term compression of the bulk C-S-H gel is further supported by the decreases of the high RH hysteresis and cavitating water content captured by the short-term sorption isotherms for samples from W55-sat to SDS40, as shown in Fig. 1. Once the compression stresses acting on the bulk C-S-H gel are absent, the gel volume is partially regained, as documented by the increase in the high RH hysteresis as well as the cavitating water content in the range of SDS11-40. The removal of water-related compression on the bulk C-S-H associated with an increase in the gel pore volume is depicted as State *IV* in Fig. 11. Finally, it should be noted that even the viscous portion of the bulk C-S-H gel rearrangement can be reversed, as was shown using samples that were first dried for several months and then re-humidified at a high RH [79].

For engineering purposes, the drying is often evaluated using the apparent water diffusion coefficient, which combines the contributions of each transport mechanism of the multi-phase model into a single RH-dependent coefficient. To account for the drying-induced microstructural rearrangement, Eq. (2) implies that the apparent water diffusion coefficient is not only a function of RH but depends on the RH history and the drying time.

5. SUMMARY AND CONCLUSIONS

The water desorption isotherms of hardened cement paste measured by different techniques were reviewed and analyzed in this study. Comparing techniques with different experimental durations demonstrated that the water content depends on both the relative humidity and ongoing changes in the porous system's characteristics such as the specific surface area. In other words, if a sample is subjected to drying conditions, the water content in the material is established considering both the thermodynamic equilibrium and microstructural rearrangement. The microstructural rearrangement rate is slower than the advection/diffusion-driven drying due to slow water flow through narrow C-S-H interlayer spaces, which causes a delayed decrease of water content at a nearly constant relative humidity.

For ease of numerical modeling, rapid desorption isotherms measured on samples with a well-equilibrated microstructure were fitted with the GAB equation extended by an activation term that accounts for the sudden decrease in water content due to cavitation. The extended GAB equation can fit the measured desorption isotherm throughout the entire range of tested relative humidities well. This desorption isotherm model was implemented into a multiphase water transport code to model the drying kinetics of hardened cement paste. The numerical results agree well with both the short- and long-term experimental data. Furthermore, the results demonstrate anomalous desorption behavior mainly for the samples dried in the range from 33 to 58 % relative humidity, which agrees with the experimental observations.

The results presented in this study suggest that the anomalous desorption kinetics of hardened cement paste originates from the colloidal nature of the bulk C-S-H gel, which is continuously altered by the compression forces related to the presence of water in the porous body.

CREDIT AUTHORSHIP CONTRIBUTION STATEMENT

Jiří Rymeš: methodology, software, validation, investigation, writing - original draft, visualization

Ippei Maruyama: project administration, supervision, conceptualization, methodology, funding acquisition, writing – review & editing

Abudushalamu Aili: validation, methodology, writing – review & editing

ACKNOWLEDGMENTS

This work was conducted with the financial support of Grant JSPS Kakenhi 18H03804 and in collaboration with Chubu Electric Power Co. Inc. The authors thank prof. Matthieu Vandamme (École des Ponts ParisTech) for fruitful discussions on the topic of creep mechanism and for initiating the analysis of kinetics data from the volumetric measurements.

APPENDIX A: MOISTURE TRANSPORT MECHANISM

Concrete is assumed here as a multiphase medium composed of solid, liquid, and gas phases. Furthermore, the solid phase is comprised of aggregate and HCP, and the gas phase is assumed to be a binary mixture of dry air and water vapor, referred to together as wet air. The transport mechanisms of each phase in such a multiphase system have been well described in the literature [e.g., 1,2]. Under pressure gradients, the water in the liquid phase or the water vapor molecules in the gas phase are transported by the advection mechanism, obeying Darcy's law. If there is a gradient in relative humidity (i.e., uneven distribution of water molecules within the wet air), the water molecules will diffuse from the dense to the less dense regions according to Fick's law. It is worth mentioning that this approach does not explicitly assume the validity of the atmospheric pressure hypothesis [67], i.e., the total gas pressure in the porous body does not necessarily equal the atmospheric pressure.

The general mass conservation law for fluid *i* is given by

$$\frac{\partial \rho_i}{\partial t} + \nabla(\rho_i \cdot \boldsymbol{v_i}) = \dot{\xi}_i \ , \tag{A.1}$$

where t is the time [s], ρ_i is the density of phase i [kg/m^3], v_i is the velocity of phase i [m/s], $\dot{\xi}_i$ is the volumetric mass generation of phase i [kg/m^3/s], and the index i denotes either the liquid phase (l), water vapor (v), dry air (d), or wet air (w). For the water transport, the right-hand side term in Eq. (A.1) represents an evaporation flux, which is positive if the liquid evaporates and negative for condensation. Hence,

$$\dot{\xi}_v = \dot{\xi}_{evp} = -\dot{\xi}_{con} \ , \tag{A.2}$$

where $\dot{\xi}_{evp}$ and $\dot{\xi}_{con}$ represent the volumetric evaporation and volumetric condensation [kg/m^3/s], respectively. The mass concentrations (volumetric masses) of each phase in the porous body can be determined based on their occupancy of the common porous space, given as

$$m_l = \rho_l \, \emptyset \, S \ , \tag{A.3}$$

$$m_w = \rho_w \, \emptyset \, (1 - S) \ , \tag{A.4}$$

$$m_v = \rho_v \, \emptyset \, (1 - S) \ , \tag{A.5}$$

where m_i is the mass concentration [kg/m^3], $\emptyset$ is the porosity [-], and S is the saturation [-].

An advection transport of a fluid through a porous system due to a pressure gradient describes Darcy's law, which states for the liquid phase and wet air,

$$\emptyset \, S \, \boldsymbol{v_l} = -\frac{K}{\eta_l} \, k_l \, grad(p_l) \ , \tag{A.6}$$

$$\emptyset \, (1 - S) \, \boldsymbol{v_w} = -\frac{K}{\eta_w} \, k_w \, grad(p_w) \ , \tag{A.7}$$

where K is the intrinsic (absolute) permeability of the porous system [m^2], k_i is the relative permeability of phase i [-], η_i is the dynamic viscosity of phase i [Pa·s], and p_i is the pressure of phase i [Pa]. Finally, diffusion governs the mass transport of water vapor within wet air, described by

$$\emptyset \, (1 - S) \, \boldsymbol{v_v} = \emptyset \, (1 - S) \, \boldsymbol{v_w} - \frac{D}{C_v / C_w} f_D \, grad\left(\frac{C_v}{C_w}\right) \ , \tag{A.8}$$

where D is the water vapor diffusion coefficient [m^2/s], C_i is the molar fraction of phase i [mol/mol], and f_D is the resistance factor of the diffusion process [-], which depends on the tortuosity of the diffusion path and for practical calculations can be evaluated as a function of $\emptyset$ and S [67].

In case of a 1D problem, inserting Eq. (A.6), (A.7), and (A.8) into Eq. (A.1) and substituting for mass concentrations from Eq.(A.3), (A.4), and (A.5) results in three transport laws for liquid phase, wet air, and water vapor:

$$\frac{\partial m_l}{\partial t} = \frac{\partial}{\partial x}\left(\rho_l \frac{K}{\eta_l}\, k_l \frac{\partial p_l}{\partial x}\right) - \xi_{evp} \ , \tag{A.9}$$

$$\frac{\partial m_w}{\partial t} = \frac{\partial}{\partial x}\left(\rho_w \frac{K}{\eta_w}\, k_w \frac{\partial p_w}{\partial x}\right) + \xi_{evp} \ , \tag{A.10}$$

$$\frac{\partial m_v}{\partial t} = \frac{\partial}{\partial x}\left[\rho_v \frac{K}{\eta_w}\, k_w \, \frac{\partial p_w}{\partial x} + \rho_v \frac{D}{\left({}^{C_v}/_{C_w}\right)} f_D \frac{\partial \left({}^{C_v}/_{C_w}\right)}{\partial x}\right] + \xi_{evp} \ , \tag{A.11}$$

where x is the distance coordinate [m].

The governing equations are completed by the two equations of state. First, the thermodynamic equilibrium at the capillary meniscus is expressed as

$$p_l = p_w - p_c \ , \tag{A.12}$$

where p_c is the capillary pressure at the meniscus [Pa], which is given by the well-known Kelvin equation as

$$p_c = -\frac{\rho_l \, R \, T}{M_l} \ln\left(\frac{p_v}{p_{sat}}\right) \ , \tag{A.13}$$

where R is the ideal gas constant [J/K/mol], T is the absolute temperature [K], M_l is the molar mass of water [g/mol], and p_{sat} is the saturation pressure of water vapor [Pa]. The second equation of state is the sorption isotherm of the material, which relates the water content and equilibrium water vapor pressure at a given temperature. It can be given either in terms of water content or in terms of saturation as

$$m_l(p_v, T, t) \ \text{ or } \ S(p_v, T, t) \ , \tag{A.14}$$

where t is the drying time [s].

APPENDIX B: NUMERICAL IMPLEMENTATION

The multiphase model was implemented using the finite difference method (FDM) with central, second-order accurate spatial discretization and fully explicit, first-order accurate time discretization. Neumann boundary conditions were used to describe the flux of each phase through the boundary using the fictitious node concept. In this approach, the boundary flux depends on the gradient between the boundary node and the external environment, while the spacing of the fictitious nodes is a fitting parameter depending on experimental conditions such as the velocity of the surrounding air and surface roughness. For each set of experimental data used for the validation of the numerical code in Section 3, the spacing of the fictitious nodes was determined by fitting the initial slope of the mass loss curve.

The multiphase approach for solving the moisture transport is strongly nonlinear due to the interaction between the liquid and the gas phases. As the liquid phase moves through the porous space, the gas pressure dramatically changes due to the volume being emptied or filled by the liquid phase. The solution method given here is based on Problem II in [68]. The convergence is achieved using a staggered iteration routine with two nested loops.

The computational algorithm is schematically illustrated in Fig. B.1. First, the advection flow of the wet air and the water vapor diffusion are calculated within the inner gas iteration loop according to the Eq. (A.10) and (A.11), respectively, until the thermodynamic equilibrium from the viewpoint of Eq. (A.12) is satisfied. The convergence is achieved by adjusting the evaporation flux. The sum of Eq. (A.9) and (A.10) gives the total mass conservation, which is solved within the mass conservation iteration loop. In the third step, the global convergence between the inner gas loop and the inner total mass conservation loop is checked using the sorption isotherm model represented by Eq. (A.14), and the thermodynamic equilibrium at the

capillary meniscus is evaluated from Eq. (A.12). The global convergence between the two inner iteration loops is achieved by adjusting the evaporation flux.

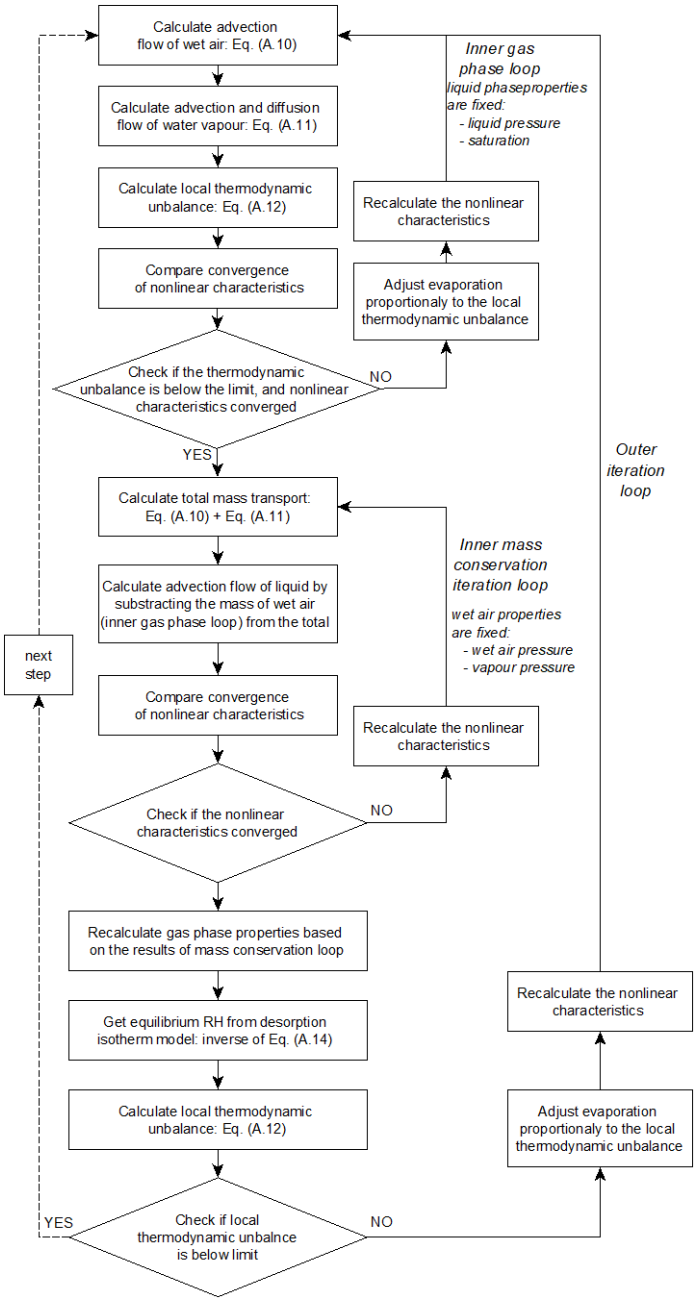

Fig. B.1 Algorithm for the numerical solution of the moisture transport.

APPENDIX C: FORMULATION OF THE FD MODEL

It is assumed that the pores, which are irreversibly lost due to the first drying (FD), are cylindrical with various radii following the Rayleigh distribution curve,

$$f(r_{FD}) = 2\left(r_{FD} - R_{0,FD}\right) e^{-\frac{\left(r_{FD}-R_{0,FD}\right)^2}{2\,\sigma_{FD}^2}} \quad , \tag{C.1}$$

where r_{FD}, $R_{0,FD}$, and σ_{FD} are the radius [nm], the smallest pore radius [nm], and the scale parameter [nm] of the FD model, respectively. The choice of this distribution is motivated by its ability to capture non-symmetric data and its well-defined limits. Furthermore, this function was used by other investigators to fit the pore size distribution [80,81]. The saturation of the FD pores is given by

$$S_{FD}(r_{FD}) = \int_{R_0}^{\infty} l_{FD}\,\pi\, f(r_{FD})^2 \; dr_{FD} = l_{FD}\,\pi^{\frac{3}{2}}\,\sigma_{FD}^3 \quad , \tag{C.2}$$

where S_{FD} is the saturation of the FD pores and l_{FD} is the total length of the FD pores [nm]. The maximum saturation of FD pores must be 1, and thus l_{FD} yields to

$$l_{FD} = \frac{1}{\pi^{\frac{3}{2}}\,\sigma_{FD}^3} \quad . \tag{C.3}$$

Substituting Eq. (C.3) in Eq. (C.1) gives the distribution function for the saturation of the FD pores in the form of

$$S_{FD} = \frac{4\left(r_{FD} - R_{0,FD}\right)^2}{\sqrt{\pi}\,\sigma_{FD}^3}\, e^{-\frac{\left(r_{FD}-R_{0,FD}\right)^2}{\sigma_{FD}^2}} \quad . \tag{C.4}$$

A cylindrical pore of a given diameter remains saturated until there is a meniscus on the liquid phase. Therefore, the volume of saturated FD pores at a given RH can be evaluated by

integrating over the pores, which have a smaller radii than the largest pore with a water meniscus. Therefore,

$$S_{FD} = \int_{R_{0,FD}}^{R_c} \frac{4\left(r_{FD} - R_{0,FD}\right)^2}{\sqrt{\pi}\,\sigma_{FD}^3}\, e^{-\frac{\left(r_{FD}-R_{0,FD}\right)^2}{2\,\sigma_{FD}^2}}\, dr$$
$$= \left[\frac{2\left(R_{0,FD} - R_c\right)}{\sqrt{\pi}\,\sigma_{FD}}\, e^{-\frac{\left(R_{0,FD}-R_c\right)^2}{\sigma_{FD}^2}}\, \mathrm{erf}\left(\frac{R_c - R_{0,FD}}{\sigma_{FD}}\right)\right] \quad , \tag{C.5}$$

where R_c is the critical pore diameter [nm] and erf is the error function. The theoretical model assumes that as the meniscus recedes due to decreasing RH, the FD pores collapse and no longer contribute to the water content. This does not agree with the actual situation, as even though some pore volume is lost due to the pore collapse, the water can still be adsorbed on the walls of these pores, thus adding to the total water content. However, as the FD model is combined with the experimental data, the water adsorbed on the walls of the collapsed pores is not considered by the theoretical model since the experimental measurements would already capture this adsorption.

The critical pore diameter, where a meniscus is still present at a given RH, is given by

$$R_c = r_k + t_{ads} \quad , \tag{C.6}$$

where r_k is the radius of the meniscus between the liquid and gas phase [nm], and t_{ads} is the thickness of adsorbed water on the pore wall [nm]. The meniscus is described by the Kelvin equation as,

$$\Delta p = \frac{R\,T}{V_{H2O}} \ln\left(\frac{p_{vap}}{p_{sat}}\right) \quad , \tag{C.7}$$

where R is the universal gas constant (J/K/mol), T is the absolute temperature (K), $V_{,H2O}$ is the molar volume of water (m^3/mol), p_{vap} is the water vapor pressure [Pa], p_{sat} is the saturated water vapor pressure [Pa], and Δp is the pressure difference between the liquid and vapor phases [Pa],

which can be found using the Young-Laplace equation. In the case of a spherical meniscus in a cylindrical pore

$$\Delta p = \gamma_{H2O}\left(\frac{1}{r_1}+\frac{1}{r_2}\right) = \frac{2\,\gamma_{H2O}}{r_k} \qquad (r_k = r_1 = r_2) \quad , \tag{C.8}$$

where γ_{H2O} is the surface tension of water [N/m], and r_1 and r_2 are two equal principal radii of the spherical meniscus [nm]. By combining Eq. (C.7) and (C.8), r_k can be found as a function of RH as

$$r_k = \frac{2\,\gamma_{H2O}\,V_{H2O}}{R\,T\,\ln\left(\frac{p_{vap}}{p_{sat}}\right)} \quad . \tag{C.9}$$

The second term in the right-hand-side of Eq. (C.6) can be calculated based on the number of adsorbed water layers n [-] and the thickness of a single water layer t_{H2O} [nm] as

$$t_{ads} = n\,d_{H2O} \quad , \tag{C.10}$$

where d_{H2O} depends on the surface-covering cross-section of a water molecule and the density of bulk water, and is given as

$$d_{H2O} = \frac{V_{H2O}}{S_{H2O}\,N_A} = \frac{M_{H2O}}{\rho_{H2O}\,S_{H2O}\,N_A} \quad , \tag{C.11}$$

where S_{H2O} is the surface-covering cross-section of a water molecule [m], N_A is the Avogadro constant (mol^{-1}), M_{H2O} is the molar mass of water [g/mol], and ρ_{H2O} is the density of liquid water [g/m^3].

Finally, assuming that the water covers the surfaces of the first drying pores in the same manner as in the rest of the HCP, the number of adsorbed water layers can be evaluated using the GAB equation as

$$n = \frac{w}{w_m} = \frac{C\ k\ h}{(1 - k\ h)[1 + (C - 1)\ k\ h]} \quad . \tag{C.12}$$

If the GAB and FD models are combined, the total water content at a given RH can be calculated as

$$w = w_{GAB} + w_{FD} \quad , \tag{C.13}$$

where w_{GAB} and w_{FD} are the water contents [mg/g-dry HCP] given by the GAB and FD model, respectively. The total pore saturation based on the GAB and FD models gives

$$S = S_{GAB}(1 - \emptyset_{FD}) + S_{FD}\emptyset_{FD} \quad , \tag{C.14}$$

where S and S_{FD} are the total and FD pore saturations [-], respectively, and $\emptyset_{FD}$ is the relative volume of FD pores with respect to the total porosity [-].

For the numerical results presented in chapter 3, the total volume fraction of FD pores was taken as 0.156, $R_{0,FD}$ = 0.75 nm, and σ_{FD} = 1.4 nm. These values were obtained by comparing the water content given by the sum of the extended GAB and FD models with the experimental data.

884 **REFERENCES**

885

886 [1] H. Sasano, I. Maruyama, A. Nakamura, Y. Yamamoto, M. Teshigawara, Impact of
887 Drying on Structural Performance of Reinforced Concrete Shear Walls, J. Adv. Concr.
888 Technol. 16 (2018) 210–232. https://doi.org/10.3151/jact.16.210.

889 [2] I. Maruyama, H. Sasano, Y. Nishioka, G. Igarashi, Strength and Young's modulus
890 change in concrete due to long-term drying and heating up to 90 °C, Cem. Concr. Res.
891 66 (2014) 48–63. https://doi.org/10.1016/j.cemconres.2014.07.016.

892 [3] I. Maruyama, Y. Nishioka, G. Igarashi, K. Matsui, Microstructural and bulk property
893 changes in hardened cement paste during the first drying process, Cem. Concr. Res. 58
894 (2014) 20–34. https://doi.org/10.1016/j.cemconres.2014.01.007.

895 [4] P. Suwanmaneechot, A. Aili, I. Maruyama, Cement and Concrete Research Creep
896 behavior of C-S-H under different drying relative humidities : Interpretation of
897 microindentation tests and sorption measurements by multi-scale analysis, Cem. Concr.
898 Res. 132 (2020) 106036. https://doi.org/10.1016/j.cemconres.2020.106036.

899 [5] R. Kurihara, I. Maruyama, Effects of heating and drying on the strength and stiffness of
900 high-early-strength Portland cement pastes, Cem. Concr. Compos. 106 (2020) 103455.
901 https://doi.org/10.1016/j.cemconcomp.2019.103455.

902 [6] J. Rymeš, I. Maruyama, R. Shimamoto, A. Tachibana, Y. Tanaka, S. Sawada, Y.
903 Ichikawa, O. Kontani, Long-term Material Properties of a Thick Concrete Wall Exposed
904 to Ordinary Environmental Conditions in a Nuclear Reactor Building : the Contribution
905 of Cement Hydrates and Feldspar Interaction, J. Adv. Concr. Technol. 17 (2019) 195–
906 215. https://doi.org/10.3151/jact.17.5.195.

907 [7] I. Maruyama, J. Rymeš, A. Aili, S. Sawada, O. Kontani, S. Ueda, R. Shimamoto, Long-
908 term use of modern Portland cement concrete: The impact of Al-tobermorite formation,
909 (2020).

910 [8] G. Pickett, Shrinkage stresses in concrete, J. Am. Concr. Inst. (ACI Proc. Vol. 42). 17
911 (1946) 165–204.

912 [9] G. Pickett, Shrinkage stresses in concrete (Part 2), J. Am. Concr. Inst. (ACI Proc. Vol.
913 42). 17 (1946) 361–398.

914 [10] Z.P. Bažant, L.J. Najjar, Nonlinear water diffusion in nonsaturated concrete, Matériaux
915 Constr. 5 (1972) 3–20. https://doi.org/10.1007/BF02479073.

916 [11] J.R. Philip, D.A. de Vries, Moisture movement in porous materials under temperature
917 gradients, Eos, Trans. Am. Geophys. Union. 38 (1957) 222–232.
918 https://doi.org/10.1029/TR038i002p00222.

919 [12] Y. Mualem, A New Model for Predicting the Hydraulic Conductivity of Unsaturated
920 Porous Media, Water Resour. Res. 12 (1976).
921 https://doi.org/10.1029/WR012i003p00564.

922 [13] M.T. van Genuchten, A closed-form equation for predicting the hydraulic conductivity
923 of unsaturated soils, Soil Sci. Soc. Am. J. 44 (1980) 892–898.
924 https://doi.org/doi:10.2136/sssaj1980.03615995004400050002x.

925 [14] C.R. Faust, Transport of Immiscible Fluids Within and Below the Unsaturated Zone: A
926 Numerical Model, Water Resour. Res. 21 (1985) 587–596.

927 [15] B.E. Sleep, J.F. Sykes, Compositional simulation of groundwater contamination by
928 organic compounds: 1. Model development and verification, Water Resour. Res. 29

(1993) 1697–1708. https://doi.org/10.1029/93WR00283.

[16] B.A. Schrefler, Multiphase flow in deforming porous material, Int. J. Numer. Methods Eng. 60 (2004) 27–50. https://doi.org/10.1002/nme.953.

[17] S. Dal Pont, F. Meftah, B.A. Schrefler, Modeling concrete under severe conditions as a multiphase material, Nucl. Eng. Des. 241 (2011) 562–572. https://doi.org/10.1016/j.nucengdes.2010.04.015.

[18] H. Cheikh Sleiman, M. Briffaut, S. Dal Pont, A. Tengattini, B. Huet, Influence of common simplifications on the drying of cement-based materials up to moderate temperatures, Int. J. Heat Mass Transf. 150 (2020). https://doi.org/10.1016/j.ijheatmasstransfer.2019.119254.

[19] R. Kiran, H. Samouh, A. Matsuda, G. Igarashi, S. Tomita, K. Yamada, I. Maruyama, Water uptake in OPC and FAC mortars under different temperature conditions, J. Adv. Concr. Technol. 19 (2021) 168–180. https://doi.org/10.3151/jact.19.168.

[20] D. Dauti, A. Tengattini, S. Dal Pont, N. Toropovs, M. Briffaut, B. Weber, Analysis of moisture migration in concrete at high temperature through in-situ neutron tomography, Cem. Concr. Res. 111 (2018) 41–55. https://doi.org/10.1016/j.cemconres.2018.06.010.

[21] M.H. Moreira, S. Dal Pont, R.F. Ausas, T.M. Cunha, A.P. Luz, V.C. Pandolfelli, Direct comparison of multi and single-phase models depicting the drying process of refractory castables, Open Ceram. 6 (2021) 100111. https://doi.org/10.1016/j.oceram.2021.100111.

[22] O. Coussy, Mechanics and physics of porous solids, John Wiley & Sons, 2010.

[23] P.J.M. Monteiro, G. Geng, D. Marchon, J. Li, P. Alapati, K.E. Kurtis, M.J.A. Qomi, Advances in characterizing and understanding the microstructure of cementitious

materials, Cem. Concr. Res. 124 (2019) 105806. https://doi.org/10.1016/j.cemconres.2019.105806.

[24] R.F. Feldman, P.J. Sereda, A model for hydrated Portland cement paste as deduced from sorption-length change and mechanical properties, Matériaux Constr. 1 (1968) 509–520. https://doi.org/10.1007/BF02473639.

[25] T.C. Powers, T.L. Brownyard, Studies of the physical properties of hardened Portland cement paste, in: Bull. 22, Research Laboratories of the Portland Cement Association, reprinted from Journal of American concrete institute, Chicago, 1948: pp. 101–132, 249–336, 469–504, 549–602, 669–712, 845–8.

[26] H.M. Jennings, Model for the microstructure of calcium silicate hydrate in cement paste, Cem. Concr. Res. 30 (2000) 101–116. https://doi.org/10.1016/S0008-8846(99)00209-4.

[27] H.M. Jennings, Refinements to colloid model of C-S-H in cement: CM-II, Cem. Concr. Res. 38 (2008) 275–289. https://doi.org/10.1016/j.cemconres.2007.10.006.

[28] W.A. Gutteridge, L.J. Parrott, A study of the changes in weight, length and interplanar spacing induced by drying and rewetting synthetic CSH (I), Cem. Concr. Res. 6 (1976) 357–366. https://doi.org/10.1016/0008-8846(76)90098-3.

[29] A. Aili, I. Maruyama, Review of Several Experimental Methods for Characterization of Micro - and Nano - Scale Pores in Cement - Based Material, Int. J. Concr. Struct. Mater. 14 (2020) 1–18. https://doi.org/10.1186/s40069-020-00431-y.

[30] I. Maruyama, N. Sakamoto, K. Matsui, G. Igarashi, Microstructural changes in white Portland cement paste under the first drying process evaluated by WAXS, SAXS, and USAXS, Cem. Concr. Res. 91 (2017) 24–32. https://doi.org/10.1016/j.cemconres.2016.10.002.

[31] L.J. Parrott, W. Hansen, R.L. Berger, Effect of first drying upon the pore structure of hydrated alite paste, Cem. Concr. Res. 10 (1980) 647–655.

[32] I. Maruyama, Y. Nishioka, G. Igarashi, K. Matsui, Microstructural and bulk property changes in hardened cement paste during the first drying process, Cem. Concr. Res. 58 (2014) 20–34. https://doi.org/10.1016/j.cemconres.2014.01.007.

[33] L. Monteilhet, J.P. Korb, J. Mitchell, P.J. McDonald, Observation of exchange of micropore water in cement pastes by two-dimensional T2 - T2 nuclear magnetic resonance relaxometry, Phys. Rev. E - Stat. Nonlinear, Soft Matter Phys. 74 (2006) 1–9. https://doi.org/10.1103/PhysRevE.74.061404.

[34] I. Maruyama, T. Ohkubo, T. Haji, R. Kurihara, Dynamic microstructural evolution of hardened cement paste during first drying monitored by 1 H NMR relaxometry, Cem. Concr. Res. 122 (2019) 107–117. https://doi.org/10.1016/j.cemconres.2019.04.017.

[35] H. Rahoui, I. Maruyama, M. Vandamme, J. Pereira, M. Mosquet, Impact of an SRA (hexylene glycol) on irreversible drying shrinkage and pore solution properties of cement pastes, Cem. Concr. Res. 143 (2021) 106227. https://doi.org/10.1016/j.cemconres.2020.106227.

[36] C. Hall, Anomalous diffusion in unsaturated flow: Fact or fiction?, Cem. Concr. Res. 37 (2007) 378–385. https://doi.org/10.1016/j.cemconres.2006.10.004.

[37] M. Saeidpour, L. Wadsö, Evidence for anomalous water vapor sorption kinetics in cement based materials, Cem. Concr. Res. 70 (2015) 60–66. https://doi.org/10.1016/j.cemconres.2014.10.014.

[38] J.M. de Burgh, S.J. Foster, Influence of temperature on water vapour sorption isotherms and kinetics of hardened cement paste and concrete, Cem. Concr. Res. 92 (2017) 37–55.

https://doi.org/10.1016/j.cemconres.2016.11.006.

[39] fib Model Code for Concrete Structures 2010, fib, 2013.

[40] P.J. McDonald, O. Istok, M. Janota, A.M. Gajewicz-Jaromin, D.A. Faux, Sorption, anomalous water transport and dynamic porosity in cement paste: A spatially localised 1H NMR relaxation study and a proposed mechanism, Cem. Concr. Res. 133 (2020) 106045. https://doi.org/10.1016/j.cemconres.2020.106045.

[41] Z. Wu, H.S. Wong, C. Chen, N.R. Buenfeld, Anomalous water absorption in cement-based materials caused by drying shrinkage induced microcracks, Cem. Concr. Res. 115 (2019) 90–104. https://doi.org/10.1016/j.cemconres.2018.10.006.

[42] C. Hall, Capillary imbibition in cement-based materials with time-dependent permeability, Cem. Concr. Res. 124 (2019) 105835. https://doi.org/10.1016/j.cemconres.2019.105835.

[43] Z. Zhang, U. Angst, A Dual-Permeability Approach to Study Anomalous Moisture Transport Properties of Cement-Based Materials, Transp. Porous Media. 135 (2020) 59–78. https://doi.org/10.1007/s11242-020-01469-y.

[44] I. Maruyama, J. Rymeš, M. Vandamme, B. Coasne, Cavitation of water in hardened cement paste under short-term desorption measurements, Mater. Struct. 51 (2018) 159. https://doi.org/10.1371/journal.pone.0112085.

[45] I. Maruyama, G. Igarashi, Y. Nishioka, Bimodal behavior of C-S-H interpreted from short-term length change and water vapor sorption isotherms of hardened cement paste, Cem. Concr. Res. 73 (2015) 158–168. https://doi.org/10.1016/j.cemconres.2015.03.010.

[46] I. Maruyama, J. Rymeš, Temperature dependency of short-term length-change and

desorption isotherms of matured hardened cement, J. Adv. Concr. Technol. 17 (2019). https://doi.org/10.3151/jact.17.5.188.

[47] H.M. Jennings, A. Kumar, G. Sant, Quantitative discrimination of the nano-pore-structure of cement paste during drying: New insights from water sorption isotherms, Cem. Concr. Res. 76 (2015) 27–36. https://doi.org/10.1016/j.cemconres.2015.05.006.

[48] S. Poyet, Experimental investigation of the effect of temperature on the first desorption isotherm of concrete, Cem. Concr. Res. 39 (2009) 1052–1059. https://doi.org/10.1016/j.cemconres.2009.06.019.

[49] V. Baroghel-Bouny, Caractérisation microstructurale et hydrique des pâtes de ciment et des bétons ordinaires et à très hautes performances, Ecole Nationale des Ponts et Chaussées, 1994.

[50] A. Korpa, R. Trettin, The influence of different drying methods on cement paste microstructures as reflected by gas adsorption: Comparison between freeze-drying (F-drying), D-drying, P-drying and oven-drying methods, Cem. Concr. Res. 36 (2006) 634–649. https://doi.org/10.1016/j.cemconres.2005.11.021.

[51] H. Garbalińska, M. Bochenek, W. Malorny, J. von Werder, Comparative analysis of the dynamic vapor sorption (DVS) technique and the traditional method for sorption isotherms determination — Exemplified at autoclaved aerated concrete samples of four density classes, Cem. Concr. Res. 91 (2017) 97–105. https://doi.org/10.1016/j.cemconres.2016.11.001.

[52] Q. Zhou, F.P. Glasser, Thermal stability and decomposition mechanisms of ettringite at <120°C, Cem. Concr. Res. 31 (2001) 1333–1339. https://doi.org/10.1016/S0008-8846(01)00558-0.

1042 [53] M.B. Pinson, E. Masoero, P.A. Bonnaud, H. Manzano, Q. Ji, S. Yip, J.J. Thomas, M.Z.
1043 Bazant, K.J. Van Vliet, H.M. Jennings, Hysteresis from multiscale porosity: Modeling
1044 water sorption and shrinkage in cement paste, Phys. Rev. Appl. 3 (2015).
1045 https://doi.org/10.1103/PhysRevApplied.3.064009.

1046 [54] S. Poyet, S. Charles, Temperature dependence of the sorption isotherms of cement-based
1047 materials: Heat of sorption and Clausius-Clapeyron formula, Cem. Concr. Res. 39 (2009)
1048 1060–1067. https://doi.org/10.1016/j.cemconres.2009.07.018.

1049 [55] Y. Xi, Z.P. Bažant, L. Molina, H.M. Jennings, Moisture diffusion in cementitious
1050 materials Moisture capacity and diffusivity, Adv. Cem. Based Mater. 1 (1994) 258–266.
1051 https://doi.org/10.1016/1065-7355(94)90034-5.

1052 [56] M. Ben Abdelhamid, D. Mihoubi, J. Sghaier, A. Bellagi, Water Sorption Isotherms and
1053 Thermodynamic Characteristics of Hardened Cement Paste and Mortar, Transp. Porous
1054 Media. 113 (2016) 283–301. https://doi.org/10.1007/s11242-016-0694-y.

1055 [57] E.O. Timmermann, Multilayer sorption parameters: BET or GAB values?, Colloids
1056 Surfaces A Physicochem. Eng. Asp. 220 (2003) 235–260.
1057 https://doi.org/10.1016/S0927-7757(03)00059-1.

1058 [58] R.K. Schofield, General discussion, Discuss. Faraday Soc. 3 (1948) 105–106.

1059 [59] Z.P. Bažant, L. Panula, Practical prediction of time-dependent deformations of concrete
1060 - Part V: Temperature effect on drying creep, Matériaux Constr. 12 (1979) 169–174.
1061 https://doi.org/10.1007/BF02494247.

1062 [60] Z.P. Bažant, L. Panula, Practical prediction of time-dependent deformations of concrete
1063 - Part II: Basic creep, Mater. Struct. 11 (1978) 317–328.

1064 [61] J. Němeček, Creep effects in nanoindentation of hydrated phases of cement pastes, Mater.
1065 Charact. 60 (2009) 1028–1034. https://doi.org/10.1016/j.matchar.2009.04.008.

1066 [62] M. Vandamme, F.-J. Ulm, Nanoindentation investigation of creep properties of calcium
1067 silicate hydrates, Cem. Concr. Res. 52 (2013) 38–52.

1068 [63] W.R.L. da Silva, J. Němeček, P. Štemberk, Methodology for nanoindentation-assisted
1069 prediction of macroscale elastic properties of high performance cementitious composites,
1070 Cem. Concr. Compos. 45 (2014) 57–68.
1071 https://doi.org/10.1016/j.cemconcomp.2013.09.013.

1072 [64] M. Vandamme, Two models based on local microscopic relaxations to explain long-term
1073 basic creep of concrete, Proc. R. Soc. A Math. Phys. Eng. Sci. 474 (2018).
1074 https://doi.org/10.1098/rspa.2018.0477.

1075 [65] A. Aili, M. Vandamme, J.M. Torrenti, B. Masson, Is long-term autogenous shrinkage a
1076 creep phenomenon induced by capillary effects due to self-desiccation?, Cem. Concr.
1077 Res. 108 (2018) 186–200. https://doi.org/10.1016/j.cemconres.2018.02.023.

1078 [66] V. Baroghel-Bouny, M. Mainguy, T. Lassabatere, O. Coussy, Characterization and
1079 identification of equilibrium and transfer moisture properties for ordinary and high-
1080 performance cementitious materials, Cem. Concr. Res. 29 (1999) 1225–1238.
1081 https://doi.org/10.1016/S0008-8846(99)00102-7.

1082 [67] M. Mainguy, O. Coussy, V. Baroghel-Bouny, Role of air pressure in drying of weakly
1083 permeable materials, J. Eng. Mech. 127 (2001) 582–592.
1084 https://doi.org/10.1061/(ASCE)0733-9399(2001)127.

1085 [68] F. Meftah, S. Dal Pont, Staggered finite volume modeling of transport phenomena in
1086 porous materials with convective boundary conditions, Transp. Porous Media. 82 (2010)

275–298. https://doi.org/10.1007/s11242-009-9422-1.

[69] S.E. Pihlajavaara, A review of some of the main results of a research on the ageing phenomena of concrete: Effect of moisture conditions on strength, shrinkage and creep of mature concrete, Cem. Concr. Res. 4 (1974) 761–771. https://doi.org/doi.org/10.1016/0008-8846(74)90048-9.

[70] F.J. Ulm, O. Coussy, L. Kefei, C. Larive, Thermo-chemo-mechanics of ASR expansion in concrete structures, J. Eng. Mech. 126 (2000) 233–242.

[71] S. Multon, F. Toutlemonde, Effect of moisture conditions and transfers on alkali silica reaction damaged structures, Cem. Concr. Res. 40 (2010) 924–934. https://doi.org/10.1016/j.cemconres.2010.01.011.

[72] S. Poyet, A. Sellier, B. Capra, G. Thèvenin-Foray, J.-M. Torrenti, H. Tournier-Cognon, E. Bourdarot, Influence of Water on Alkali-Silica Reaction: Experimental Study and Numerical Simulations, J. Mater. Civ. Eng. 18 (2006) 588–596. https://doi.org/10.1061/(asce)0899-1561(2006)18:4(588).

[73] T.C. Powers, T.L. Brownyard, Studies of the physical properties of hardened Portland cement paste, in: Bull. 22, Research Laboratories of the Portland Cement Association, reprinted from Journal of American concrete institute, Chicago, 1948: pp. 101–132, 249–336, 469–504, 549–602, 669–712, 845–8.

[74] I. Maruyama, J. Rymeš, M. Vandamme, B. Coasne, Cavitation of water in hardened cement paste under short-term desorption measurements, Mater. Struct. Constr. 51 (2018). https://doi.org/10.1617/s11527-018-1285-x.

[75] A.C.A. Muller, K.L. Scrivener, J. Skibsted, A.M. Gajewicz, P.J. McDonald, Influence of silica fume on the microstructure of cement pastes: New insights from 1H NMR

relaxometry, Cem. Concr. Res. 74 (2015) 116–125. https://doi.org/10.1016/j.cemconres.2015.04.005.

[76] R. Sinko, M. Vandamme, Z.P. Bažant, S. Keten, Transient effects of drying creep in nanoporous solids: Understanding the effects of nanoscale energy barriers, Proc. R. Soc. A Math. Phys. Eng. Sci. 472 (2016). https://doi.org/10.1098/rspa.2016.0490.

[77] G. Geng, R.J. Myers, J. Li, R. Maboudian, C. Carraro, D.A. Shapiro, P.J.M. Monteiro, Aluminum-induced dreierketten chain cross-links increase the mechanical properties of nanocrystalline calcium aluminosilicate hydrate, Sci. Rep. 7 (2017) 1–10. https://doi.org/10.1038/srep44032.

[78] J. Frech-Baronet, L. Sorelli, J.P. Charron, New evidences on the effect of the internal relative humidity on the creep and relaxation behaviour of a cement paste by micro-indentation techniques, Cem. Concr. Res. 91 (2017) 39–51. https://doi.org/10.1016/j.cemconres.2016.10.005.

[79] R. Hafsa, Contribution to Understanding the Action of Shrinkage Reducing Admixtures in Cementitious Materials: Experiments and Modelling, Université Paris-Est, 2018.

[80] T. Ishida, K. Maekawa, T. Kishi, Enhanced modeling of moisture equilibrium and transport in cementitious materials under arbitrary temperature and relative humidity history, Cem. Concr. Res. 37 (2007) 565–578. https://doi.org/10.1016/j.cemconres.2006.11.015.

[81] Q. Huang, Z. Jiang, X. Gu, W. Zhang, B. Guo, Numerical simulation of moisture transport in concrete based on a pore size distribution model, Cem. Concr. Res. 67 (2015) 31–43. https://doi.org/doi.org/10.1016/j.cemconres.2014.08.003.